The importance of mechanical and biological cues of tympanic membrane grafts to ensure optimal regeneration

The importance of mechanical and biological cues of tympanic membrane grafts to ensure optimal regeneration

Oriana Nobus[1#], Laurens Parmentier[1#], Pieter Livens[2], Pieter Muyshondt[2], Krystyna Szewcyk[3], Christel Jacobs[3], Dorien Verdoodt[3], Leen Pieters[4], Quinten Thijssen[1], Bo Van Durme[1], Anne Vral[4], Joris Dirckx[2], Vincent Van Rompaey[3,5*] and Sandra Van Vlierberghe[1*]

[1] Polymer Chemistry and Biomaterials Group (PBM), Centre of Macromolecular Chemistry (CMaC), Ghent University, 9000 Ghent, Belgium

[2] Laboratory of Biomedical Physics (BIMEF), University of Antwerp, 2020 Antwerp, Belgium

[3] Department of Translational Neurosciences, University of Antwerp, 2610 Wilrijk, Belgium

[4] Department of Human Structure and Repair, Ghent University, 9000 Ghent, Belgium

[5] Department of Otorhinolaryngology and Head & Neck Surgery, Antwerp University Hospital, 2650 Edegem, Belgium

[#] Contributed equally

[*] *Sandra.VanVlierberghe@UGent.be* and *vincent.vanrompaey@uantwerpen.be*

Highlights

- DLP-printed biocompatible tympanic membrane grafts mimicking the *in vivo* thickness
- Optimal *in vivo* healing with superior mechanical properties and cell-interactivity

Abstract

Chronic suppurative otitis media (CSOM) is often associated with permanent tympanic membrane (TM) perforation and conductive hearing loss. The current clinical gold standard, using autografts and allografts, suffers from several drawbacks. Artificial replacement materials can help to overcome these drawbacks. Therefore, scaffolds fabricated through digital light processing (DLP) were herein created to support TM regeneration. Various UV-curable printing inks, including gelatin methacryloyl (GelMA), gelatin-norbornene-norbornene (GelNBNB) (crosslinked with thiolated gelatin (GelSH)) and alkene-functionalized poly-ε-caprolactone (E-PCL) (crosslinked with pentaerythritol tetrakis(3-mercaptopropionate) (PETA4SH)) were optimized regarding photo-initiator (PI) and photo-absorber (PA) concentrations through viscosity characterisation, photo-rheology and the establishment of working curves for DLP. Our material platform enabled the development of constructs with a range of mechanical properties (plateau storage modulus varying between 15 – 119 kPa). Excellent network connectivity for the GelNBNB and E-PCL constructs was demonstrated (gel fractions > 95%) whereas a post-crosslinking step was required for the GelMA constructs. All samples showed excellent biocompatibility (viability >93% and metabolic activity >88%). Finally, *in vivo* and *ex vivo* assessments, including histology, vibration and deformation responses measured through laser doppler vibrometry and digital image correlation respectively, were performed to investigate the effects of the scaffolds on the anatomical and physiological regeneration of acute TM perforations in rabbits. The data showed that the most efficient healing with the best functional quality was obtained when both mechanical (obtained with the PCL-based resin) and biological (obtained with the gelatin-based resins) material properties were taken into account.

Keywords

Tympanic membrane – Digital light processing – Photo-crosslinkable polymers – Digital image correlation

1. Introduction

The human ear is a complex biomechanical system which plays a crucial role in the perception of sound [1]. The TM is connected to the middle ear (ME) bones, called ossicles, and transforms acoustical energy into ossicular vibratory motion [2]. The TM is shaped like a flattened cone with the apex pointing medially. Its vertical axis ranges from 8.5 to 10 mm while the horizontal axis ranges from 8 to 9 mm (mean total area of 85 mm^2) [1]. Sound waves of frequencies between 20 – 20000 Hz (determining the pitch of the perceived sound) and pressures between 10^{-5} Pa (hearing threshold) and 100 Pa (pain threshold) (determining the intensity of the perceived sound) are optimally transmitted, through vibrations of the TM, via the ossicular chain to the cochlea, where the mechanical vibrations are converted into pressure waves in the cochlear fluid [3]. Simultaneously, the TM can be subject to quasi-static pressures up to several kPa which occur, for example, during elevator travel, meteorological changes and gas exchange processes in the ME. Changes in the structure and mechanical properties of the TM due to ME disease or damage (TM perforation) can deteriorate the conduction of sound-induced vibrations to the internal ear and the associated nerve transmission, resulting in conductive hearing loss [1].

Otitis media (OM) refers to a group of complex infectious and inflammatory diseases of the ME that can be either acute or chronic [4]. The most common cause of OM is a bacterial infection of the ME. Despite appropriate antibiotic therapy, acute OM (AOM) may progress towards CSOM associated with TM perforation and purulent discharge (otorrhea). In most cases, this stage of OM is associated with permanent TM perforation and conductive hearing loss. CSOM is one of the most common chronic infectious diseases worldwide [5]. The World Health Organization (WHO) estimates that the global burden of disease from CSOM affects up to 330 million people, of which 60% suffer from significant hearing impairment.

In most cases, acute TM perforations heal spontaneously, yet large TM perforations (50 % or more of the entire TM), or those associated with chronic otorrhea, or inflammation do not heal without specific surgical treatments [6,7]. Tympanoplasty entails the surgical repair of the TM. When successfully performed, it restores sound transmission while creating a barrier between the ear canal and the ME. The most common materials used today are autologous temporalis fascia, perichondrium and cartilage, which can be harvested from the patient during surgery. However, a second surgical site must be created [8]. Furthermore, it may happen that there is no suitable grafting material left due to revision surgeries which are needed in 28 % of the cases. In this case, allograft tympano-ossicular systems (ATOS) can be used to reconstruct the defect in the TM or the ossicular mechanism. However, there are some challenges accompanying ATOS procurement: intensive training is required to enable high-quality procurement, extensive quality control of the material is needed, there exists a risk of disease transmission, and most importantly, there is a need for available donors [9,10]. Therefore, new methods for reconstructing TM perforations should be investigated as alternatives for the use of grafts, thereby considering the desired mechanical properties and biological characteristics to ensure optimal regeneration.

A crucial feature accompanying the vibration biomechanics of the TM, in addition to the collagen fiber organization, includes the thickness, since it describes the mass distribution, i.e. the inertia, of a vibrating TM and also influences the effective stiffness along with the membrane shape and the storage modulus of the membrane material [1]. Furthermore, the thickness of the human TM has been reported as a critical parameter with the most significant impact on the regenerative outcome. While

it is generally agreed that the thickness is not homogeneously distributed at different locations of the TM, a uniform value for the thickness of the human TM is usually assumed in ME models, ranging from 30 to 150 µm (average value of 74 µm) [1]. This wide range evidences the large interindividual variability of the mean thickness values and hence underlines that there is no typical human TM thickness. Studies have shown that both the epidermal and mucosal epithelia spontaneously migrate *in vivo* [2,3,11]. Based on these findings, the main requirement for neo-formation of the collagenous network is a thin TM scaffold that can act as a support for regeneration. In order to allow the production of sufficiently thin samples resembling the native TM thickness, digital light processing (DLP) is selected herein as it enables superior design control and resolution (minimum size of 50 µm) compared to previously reported fabrication methods like electrospinning or extrusion-based 3D-printing [12]. For the TM, very different elastic moduli have been reported over the years, as the values are strongly dependent on the accuracy of thickness measurements [1]. For the stress range from 0 to 1 MPa in uniaxial tensile testing, elastic moduli from 0.4 to 22 MPa have been reported [13]. *In situ* indentation measurements at a quasi-static indentation frequency of 0.2 Hz, revealed an average elastic modulus of 2.9 ± 1.3 MPa for the TM [14]. It nevertheless remains unclear whether the reported mechanical and biological properties of the native tissue should be mimicked with the applied scaffold materials.

Gelatin, derived from denatured collagen, is of specific interest when taking into account the composition of the TM extracellular matrix. The material is considered safe thanks to its approval by the food and drug administration (FDA) for use in the food and pharmaceutical industry [15]. Despite its cell-interactive and biodegradable properties, the material suffers from poor mechanical properties and instant dissolution at body temperature which compromises surgical handling and initial scaffold stability. To tackle these issues, gelatin can be functionalized with photo-crosslinkable moieties (resulting in a storage modulus up to 368 kPa) [16]. Gelatin type B derivatives, such as GelMA, can be crosslinked to form a hydrogel through radical-mediated chain-growth photo-polymerization. However, an undesirable characteristic of chain-growth polymerization is the formation of inhomogeneous networks providing limited control over the polymerized network [15]. A promising alternative for GelMA includes photo-induced thiol-ene chemistry, in which an alkene reacts with a thiolated crosslinker via a step-growth photo-polymerization mechanism [17]. This highly controlled crosslinking mechanism is characterized by a faster reaction, higher reactivity and a more homogeneous network accompanied by a higher conversion of the functional groups within a shorter period of time. Norbornene is a preferred alkene moiety due to its exceptionally rapid reaction with thiols because of ring strain relief during reaction along with limited homopolymerization [18]. In an attempt to further increase the mechanical properties through introduction of additional photo-crosslinkable moieties, gelatin-norbornene-norbornene (GelNBNB) is herein proposed since not only the native amine groups but also aminated carboxylic acids can be modified with activated norbornene carboxylic acid. These ene functionalities are then further exploited for thiol-ene click chemistry with the thiol groups from thiolated gelatin (GelSH) obtained by thiolation of the native amine groups present in gelatin (+/- 14 thiols per gelatin chain).

To further extend the range of mechanical parameters, poly-ε-caprolactone (PCL), a bioresorbable polyester, is also investigated due to its superior mechanical properties (elastic moduli ranging from 0.21 to 0.44 GPa [19]) compared to gelatin-based materials. PCL is a synthetic, hydrophobic and aliphatic polymer, part of the family of poly(α-hydroxy esters), which has been approved by the FDA for drug delivery purposes thanks to its excellent biocompatibility [20,21]. PCL is characterized by a slow degradation rate of 2-4 years (depending on the starting molar mass and the construct design) whereby its degradation product (i.e. 6-hydroxyhexanoic acid) can be resorbed *in vivo* and excreted through natural pathways when the molar mass is < 3000 g/mol [21,22]. To render PCL DLP printable, alkene end groups are introduced resulting in alkene-functionalized PCL (E-PCL) which is further combined in a thiol-ene reaction in the presence of pentaerythritol tetrakis(3-mercaptopropionate) (PETA4SH) [23].

Herein, the viscosity and mechanical properties of the different materials are carefully selected to develop three different biomaterial resins suitable for DLP printing based on either gelatin or PCL. The range in mechanical properties is optimized by varying the polymer, the PI and the PA concentration. Next, the resins are optimized by exploiting working curves to produce printed constructs with appropriate Z-axis resolution targeting a construct thickness of 100 µm while ensuring control over the XY-axis dimensions. Next, physico-chemical tests including gel fraction and swelling degree experiments are executed. Finally, the response of fibroblasts is quantified *in vitro* to assess the materials' biocompatibility. For each optimized resin, the scaffolds are assessed both *in vivo* and *ex vivo* to provide an indication of the effect of the scaffolds on the middle ear regeneration anatomy through histological analysis and function hereby investigating the vibration and deformation response under well-defined loads. The outcome is compared against both untreated perforated TMs and healthy (normal) TMs.

2. Materials and methods

2.1. Materials

Gelatin type B was kindly provided by Rousselot Belgium. Allyl isocyanate (98 %), pentaerythritol tetrakis (3-mercaptopropionate) (> 95 %; PETA4SH), dimethyl terephthalate (> 99 %; DMT), N-methyl-2-pyrrolidone (> 99 %; NMP), phosphate buffered saline (PBS), tartrazine (> 85 %), 2-mercaptoethanol (> 99 %), DL-*N*-acetylhomocysteine thiolactone (98 %), ortho-phthaldialdehyde (> 97 %; OPA), N-butylamine (99.5 %), boric acid (> 99.5 %; H_3BO_3), dimethylsulfoxide (> 99 %; DMSO), potassium chloride (99.0-100.5 %; KCl), sodium hydroxide (> 98 %; NaOH), ethylene diamine (> 99 %), monopotassium phosphate (> 99 %; KH_2PO_4), methacrylic anhydride (94 %), disodium phosphate (> 99 %; Na_2HPO_4), 5-norbornene-2-carboxylic acid (98 %), ethylenediaminetetraacetic acid (EDTA), sodium bicarbonate ($NaHCO_3$), and sodium carbonate (Na_2CO_3) were purchased at Sigma-Aldrich. Lithium bromide (LiBr) was purchased at Fluka. 1-Ethyl-3-(3-dimethylaminopropyl)carbodiimide hydrochloride (> 98 %; EDC) and tris(2-carboxyethyl)phosphine hydrochloride (TCEP) were obtained from TCI. N-hydroxysuccinimide (98 %; NHS) and PCL diol (MM 2000 g/mol) were purchased at Acros. (2,4,6-Trimethylbenzoyl)-phenylphosphinic acid ethyl ester (i.e. Speedcure TPO-L) was obtained from Lambson. Deuterated chloroform (99.8 %; $CDCl_3$) and deuterium oxide (D_2O) were supplied by Eurisotop. Bismuth neodecanoate was supplied by Allnex. Toluene p. (> 99 %) was supplied by Chemlab. The dialysis membranes Spectra/Por® (MMCO 12-14 kDa) were obtained from Polylab. Decalcifier DC2 was supplied by VWR Chemicals. All chemicals were used as received unless stated otherwise.

2.2. Development of photo-crosslinkable polymers

2.2.1. GelMA

Gelatin methacryloyl (GelMA) was developed as described earlier by Van den Bulcke *et al* [24]. In brief, 2.5 eq methacrylic anhydride with respect to the amines present in gelatin type B were added to 10 w/v% dissolved gelatin type B in phosphate buffer (pH 7.8) at 40°C. Thereafter, the reaction mixture was stirred for 1 h, and 1 L of double distilled water (DDW) was added to the mixture. The solution was transferred to dialysis membranes and was dialyzed against distilled water for 24 h at 40°C. The water was changed 5 times during the 24 h. Following dialysis, the pH was set at 7.4 and the solution was transferred to petri-dishes, frozen at -20°C and dried in the freeze-dryer.

A UvikonXL UV-visible (UV-Vis) spectrophotometer from BIO-TEK instruments (LabPowerv4 software) was used to determine the degree of substitution (DS) of the gelatin derivatives via an ortho-phthalic dialdehyde (OPA) spectrophotometric assay. In brief, n-butylamine (0.002 M, 0.004 M, 0.006 M or 0.01 M) standards together with a 2-mercaptoethanol solution and an OPA stock solution were subsequently added to a PMMA cuvette and were mixed. Finally, the absorbance was measured at 335 nm (at 37°C) and was compared to a blank (with DDW instead of the standard) to obtain a calibration

curve. A zero measurement (3 blank samples) was performed to rule out background interference. Similar measurements were performed with the modified gelatin solution. All measurements were performed in triplicate. Calculation of the number of free amine groups, remaining after the modification, enabled the indirect determination of the modification degree of gelatin:

$$\mathrm{DS}(\%) = \left(\frac{\mathrm{n}_{\mathrm{NH}_2 Gel} - \mathrm{n}_{\mathrm{NH}_2 GelMA}}{\mathrm{n}_{\mathrm{NH}_2 Gel}}\right) * 100$$

with n_{NH2Gel} the number of amines present in gelatin type B (0.385 mmol amines/g gelatin) and $n_{NH2GelMA}$ the number of amines present in gelatin type B modified with methacryloyl moieties. The DS of GelMA as determined through the OPA assay was 99 %.

2.2.2. GelNBNB

Norbornene-norbornene-modified gelatin (GelNBNB) was developed by adding 1 eq of 1,2-diaminoethane with respect to the carboxylic acids present in gelatin type B in combination with 5 w/v% gelatin type B in phosphate buffer at 40°C followed by 2 eq EDC and 3 eq NHS. After overnight reaction, the flask was diluted with an equal volume of double distilled water. The solution was transferred to dialysis membranes and was dialyzed against distilled water during 24 h at 40°C during which the water was changed 5 times. Following dialysis, the pH was set at 7.4 and the aminated gelatin solution was transferred to petri-dishes, frozen at -20°C and dried in the freeze-dryer. Before continuing to the next step, the amine content was analyzed using an OPA spectrophotometric assay and was found to be 0.582 mmol amines/g gelatin. Then, 1.2 eq of activated 5-norbornene-2-carboxylic acid compared to the total amine content in aminated gelatin were added to 3.33 w/v% aminated gelatin in dried DMSO (vacuum distillation using calcium hydride as drying agent) at 50°C. After 15 h reaction under inert atmosphere, the reaction was precipitated in a tenfold excess of acetone and filtered. Thereafter, the precipitate was redissolved in DDW, and the solution was transferred to dialysis membranes. Following dialysis, the pH was set at 7.4 and the GelNBNB solution was transferred to petri-dishes, frozen at -20°C and dried in the freeze-dryer. The DS of GelNBNB was calculated through:

$$\mathrm{DS}(\%) = \left(\frac{\mathrm{n}_{\mathrm{NH}_2 AmGel} - \mathrm{n}_{\mathrm{NH}_2 GelNBNB}}{\mathrm{n}_{\mathrm{NH}_2 Gel}}\right) * 100$$

with n_{NH2Gel} the number of amines present in gelatin type B (0.385 mmol amines/g gelatin), $n_{NH2AmGel}$ the number of amines present in aminated gelatin and $n_{NH2GelNBNB}$ the number of amines present in aminated gelatin type B modified with norbornene moieties. This finally resulted in a DS of 147 % with respect to the amines present in pristine gelatin.

2.2.3. GelSH

Thiolated gelatin (GelSH) was developed as described earlier by Van Vlierberghe *et al* [25]. In brief, 5 eq with respect to the amines present in gelatin type B were added to 10 w/v% dissolved gelatin type B in carbonate buffer (pH 10) at 40°C. When a homogeneous gelatin solution was obtained, EDTA (1.5 mM) was added. The reaction was stirred for 3 h at 40°C. Thereafter, the reaction mixture was diluted with 200 ml DDW followed by dialysis for 24 h. Both reaction and dialysis were performed under argon atmosphere. Finally, the pH was adjusted to 7.4 and the GelSH was frozen in liquid N_2 followed by freeze-drying. The substitution degree was quantified through:

$$\mathrm{DS}(\%) = \left(\frac{\mathrm{n}_{\mathrm{NH}_2 Gel} - \mathrm{n}_{\mathrm{NH}_2 GelSH}}{\mathrm{n}_{\mathrm{NH}_2 Gel}}\right) * 100$$

with n_{NH2Gel} the number of amines present in gelatin type B (0.385 mmol amines/g gelatin) and $n_{NH2GelSH}$ the number of amines present in gelatin type B modified with thiol groups. The DS of GelSH as determined through the OPA assay was 75 %.

2.2.4. E-PCL

30 g of PCL diol (1 eq, 15 mmol) was dried in a desiccator charged with dry silica. Thereafter, the diol was dissolved in 100 ml of anhydrous toluene in a two-neck round bottom flask equipped with a magnetic stirrer and flushed with argon so that an inert argon atmosphere was obtained. After the addition of the catalyst bismuth neodecanoate (0.028 mmol), the reaction was heated to 60°C. This was followed by the addition of an excess of allyl isocyanate (3 eq, 45 mmol). The reaction was stirred for 1 h, after which the final alkene-functionalized PCL (E-PCL) product was dried, precipitated in a tenfold excess of diethyl ether, and filtered on a glass filter.

The DS of E-PCL (10 mg) was determined using proton nuclear magnetic resonance spectroscopy (Bruker Avance 400 MHz ^{1}H-NMR spectrometer) in 1 ml $CDCl_3$ as solvent containing 10 mg DMT as internal standard. The signal intensities of the integrated peaks were compared to the peak intensities corresponding to DMT (δ = 8 ppm). The introduced alkene functionalities correspond to the characteristic signals of the alkene protons (δ = 5.2 ppm and 5.8 ppm). Then, the alkene content (mol/g) and DS were calculated (N is the number of protons of DMT and alkene endcaps):

$$Alkene\ content\ \left(\frac{\text{mol}}{\text{g}}\right) = \frac{I\ (\delta\ 5.8) + I(\delta 5.2)}{I(\delta 8)} * \frac{N(DMT)}{N(alkene)} * \frac{m(DMT)}{MM(DMT)} * \frac{1}{m(E-PCL)}$$

$$DS\ (\%) = \frac{n(alkene)}{2} * \big(MM(PCL\ diol) + (MM(allyl\ isocyanate) * 2)\big) * 100$$

The DS of E-PCL was determined to be 96 %. The ^{1}H-NMR spectrum is included in the Supplementary information (S.2.).

2.3. Digital light processing

2.3.1. UV-VIS spectroscopy

A Shimadzu's UV-1900i with LabSolutions software was used to perform UV-VIS spectrophotometry. One PMMA cuvette was filled with a reference solution (NMP or PBS) and another with the solution that needed to be examined. A baseline was recorded with the reference cuvette. Next, the cuvette containing the sample was placed in the instrument and an AutoZero measurement was performed at 580 nm to set the absorbance level to zero. A full wavelength (190 - 600 nm) scan was performed, and the measurements were done in triplicate.

2.3.2. Droplet tests

To gain preliminary insight in the crosslinking efficiency of the printing resins, droplet tests were carried out to determine the range of printing parameters in which crosslinking occurs efficiently (Supplementary information S.4.). More specifically, the printer light intensity (7.26 - 41.3 mW/cm^2), the resin exposure time (3 - 30 s), the photo-crosslinkable polymer concentration (GelMA: 10 – 30 wt% in PBS, E-PCL: 50 – 70 wt% in NMP) and the PI concentration (Li-TPO-L (GelMA): 0.01 – 2 wt%, TPO-L (E-PCL): 0.1 – 2.5 wt%) were varied.

2.3.3. In situ photo-rheology and viscosity testing

The crosslinking kinetics were studied using a Physica MCR 301 Rheometer (Anton Paar). The chosen intensities corresponded with the applied printer intensities that were deducted from the droplet tests (Table 1). Crosslinking of the gelatin inks (GelMA and GelNBNB) was performed with UVA-light with a wavelength of 365 nm, and an intensity of ~20 mW/cm^2 (EXFO Novacure 2000 UV-light source). Crosslinking of the E-PCL ink was also performed with UVA-light at an intensity of ~30 mW/cm^2. The measurements were performed within the linear viscoelastic range of gelatin at 0.1 % strain, a normal force of 1 N, an oscillation frequency of 1 Hz, and at 37°C. In the case of E-PCL, similar settings were used, except for the temperature which was set at 20°C. The UV-light was turned on automatically

after 60 sec, and the sample was exposed for 60 sec (60 points). Then, the UV-light was turned off and 10 points (120 sec) were measured. The measurements were done in triplicate. Viscosity testing was performed without UVA-light exposure. A shear rate of 1 s^{-1} at 37°C was applied for the gelatins (GelMA and GelNBNB) and at 20°C for E-PCL. 40 points were measured with a total duration of 10 min for each measurement. The measurements were executed in triplicate.

2.3.4. Resin preparation and DLP printing

3D printing of gelatin resins was performed on a LumenX+ DLP printer, the heating plate was set at 37°C and the intensity was set at 19.51 mW/cm^2. Before printing, the building plate was slightly heated to avoid physical gelation during printing. For the GelNBNB resins, the vials were flushed with and shaken three times after opening of the vial to prevent the formation of disulfide bonds due to exposure to O_2. The equivalents of TCEP (0.5 eq) were chosen with respect to the molar amount of thiols present in the solution. 3D printing of E-PCL resins was performed on a LumenX DLP printer, and the intensity was set at 29.52 mW/cm^2. Li-TPO-L and TPO-L were used as PI for the gelatins and E-PCL respectively (Supplementary information S.1.). The PI concentrations were 2, 9 and 10 mol% for 15 wt% GelNBNB, 30 wt% GelMA and 70 wt% E-PCL respectively. All scaffolds were fabricated using a step size of 50 µm.

The concentration of thiol groups was chosen to be equimolar with respect to the crosslinkable 'ene' moieties present in GelNBNB and E-PCL. The total concentration was based on the combined mass of the photo-crosslinkable material and its thiolated crosslinker. The choice of resin compositions was based on droplet tests, viscosity testing and photo-rheology (Table 1). All CAD designs used during printing were made using SolidWorks 2021.

Table 1: Overview of printing inks used for final *in vivo* evaluation.

	Thiolated crosslinker	*PI**	*PA***	*Solvent*	*Intensity*
15 wt% GelNBNB	GelSH + 0.5 eq TCEP	0.1 wt%	0.001 wt%	PBS	19.51 mW/cm^2
30 wt% GelMA	/	1 wt%	0.001 wt%	PBS	19.51 mW/cm^2
70 wt% E-PCL	PETA4SH	2.5 wt%	0.01 wt%	NMP	29.52 mW/cm^2

**wt% PI calculated based on wt% photo-crosslinkable material*

***wt% PA calculated based on wt% PI*

2.3.5. Working curve determination

For each sample made at a specific energy dose (mJ/cm^2), 4 images were captured, and 5 measurements were made per image. The average thickness of the samples together with the standard deviation (SD) for each applied energy dose were applied to establish the working curves. The curves were the result of plotting the average thickness against the applied energy dose in a semi-logarithmic plot. A regression line was fitted through these points and the slope of this regression line was used to estimate the characteristic curing depth (D_p). The critical energy dose (E_c) was estimated by the intersection of the fitted line with the X-axis. These resin characteristics could then be used to determine the relationship between the applied energy dose and the resulting curing depth for each resin composition.

2.3.6. Optical microscopy

An optical microscope (Zeiss Axiotech 100 HD/DIC) with Zen core software was used to measure the thickness, pore size and strut size of printed samples at 5x magnification.

2.4. Physico-chemical testing through gel fraction, swelling degree determination and frequency sweep testing

The dimensions of the four DLP printed samples were 0.8 mm in diameter with 200 µm thickness. The gel fraction is the remaining mass fraction of the polymer network after leaching out the non-crosslinked parts and is determined according to the following formula:

$$\text{Gel fraction } (\%) = \left(\frac{m_{d,2}}{m_{d,1}}\right) * 100$$

The gel fraction of the modified gelatin networks was determined by freeze-drying the disks immediately after crosslinking. Next, the dry mass of these disks was determined ($m_{d,1}$), and the films were incubated in PBS at 37°C for 24 h. After equilibrium swelling, the disks were freeze-dried, and the dry mass was determined again ($m_{d,2}$). The E-PCL disks were put in the vacuum oven at 45°C overnight. The dry mass of these disks was determined ($m_{d,1}$) and were then immersed in NMP. After 24 h, the disks were again put in the vacuum oven overnight. Afterwards, the dry mass was determined again ($m_{d,2}$).

The equilibrium swelling degree was determined by immersing dry disks in PBS for 24 h. The swollen mass (m_s) of the disks was determined. Afterwards, the samples were freeze-dried (for the modified gelatin networks) or put in the vacuum oven (for the E-PCL disks) to determine the dry mass (m_d). The swelling degree was determined using the following equation:

$$\text{Swelling degree } (\%) = \left(\frac{m_s - m_d}{m_d}\right) * 100$$

Frequency sweep testing was performed using a Physica MCR 301 Rheometer (Anton Paar) on equilibrium swollen, chemically crosslinked (a dose of 10 J/cm^2 was applied) 14 mm diameter disks in triplicate. The measurements were performed using a strain amplitude of 0.1 %, a normal force of 1 N and an oscillation frequency range of 0.5-1.95 Hz at 37°C. The storage modulus of the networks was then obtained as the ten-point average value of the storage modulus around 1 Hz.

2.5. *In vitro* evaluation

The *in vitro* biocompatibility of DLP printed disks (8 mm and 200 µm thickness) was determined. A post-curing step with UVA-light (365 nm, 10 mW/cm^2) for 15 min was implemented to ensure fully crosslinked samples. The disks were sterilized by immersing them in 70 % ethanol for 24 h, with a refreshment of the ethanol solution after 12 h, and subsequent UVC-irradiation (100 - 250 nm range, 15 mW/cm^2) for 2 h. Each sterilized disk was incubated at 37°C in 1 ml cell culture medium during 1, 14 or 28 days.

Human foreskin fibroblast cells (HFFs) were cultured at 37°C in 5 % CO_2 in cell culture medium consisting of Dulbecco's modified eagle medium (DMEM) supplemented with 10 v% fetal bovine serum (FBS) and 1 v% penicillin/streptomycin (P/S). The medium was changed every 2-3 days till reaching confluency of 80 – 90 % after which the cells were split. The cells were seeded in a 96-well plate (approximately 10^4 cells per well in 200 µl culture medium). After 24 h of cell attachment, the culture medium was removed and 200 µl of the medium that was in contact with the DLP printed disks, was placed in the wells that contained the fibroblasts. Tissue culture plastic (TCP) was used as a positive control (non-toxic). After one day of incubation, a live/dead and an 3-(4,5-Dimethylthiazol-2-yl)-5-(3-carboxymethoxyphenyl)-2-(4-sulfophenyl)-^{2}H-tetrazolium (MTS) assay were performed to determine the viability and metabolic activity of the fibroblasts respectively.

2.5.1. Live/dead assay

The cell viability was assessed by a calcein-acetoxymethyl (2 µl / ml PBS)/propidium iodide (2 µl / ml PBS) live-dead fluorescence staining in triplicate. After medium removal, 0.15 ml of the live-dead solution was added to each well. After 10 min of incubation in the dark at RT, the cells were imaged

with an inverted fluorescence microscope (IX81, Olympus) with motorised Z-axis control, CoolLED pE4000 (16 channels, 365-770 nm), an ORCA-Flash4.0LT+ cMOS camera, glass warming plate Okolab, CellSens Dimension v.3 software and air objective 4x/0.13 UPlanFLN. The microscope had a Green Fluorescent Protein (GFP) filter for the intracellular esterase-based hydrolysis product to visualize green living cells and a Texas Red (TxRed) filter for PI to visualize the red dead cells.

2.5.2. MTS assay

The MTS compound is a tetrazolium salt that is reduced by NAD(P)H-dependent dehydrogenase enzymes in viable cells into formazan. First, the stock solution MTS was thawed. The basic culture medium of the cells was discarded and refreshed with 100 µl medium. Thereafter, the MTS solution was added to the wells containing the fresh medium (20 µl). The well plates were incubated in the dark on a shaker at 37°C for 2 h. Next, 100 µl of the supernatants was added to a 96 well plate and absorbance was read at 490 nm with a spectrophotometer (BioTek Instruments; EL800 Universal Microplate Reader with GEN5 software) to analyze the metabolic activity at days 1, 14 and 28. This was done in triplicate.

2.6. *In vivo* evaluation

All animal experiments were carried out in alignment with the Guidelines for the Care and Use of Laboratory Animals. All animal experimental procedures were approved by the Ethics Committee for Animal Experiments of the University of Antwerp (approval No 2021-76). Nine female adult rabbits of the New Zealand White (NZW) strain at nine weeks of age were used to compare the DLP-printed constructs based on the three different developed biomaterial inks (3 animals/experimental group). The animals were housed in accordance with European guidelines under standard laboratory conditions. Before the start of the first experiment, the animals were given at least one week to acclimatize.

The animals were anaesthetized with ketamine (40 mg/kg) and xylazine (5 mg/kg) intramuscular (i.m.). Maintenance was ensured with 1 – 2 % isoflurane mixed with oxygen through a respirator to avoid blocking the nostrils. Glycopyrrolate (0.01 mg/kg) and carprofen (2 mg/kg) were administered subcutaneously (s.c.) as premedication to prevent airway obstruction by mucus, and as analgetic respectively. The animals were placed on a heating pad with feedback control to maintain a stable body temperature of 38 - 39°C. To prevent dehydration and corneal damage, a Duratears eye ointment was applied. Also, Hartmann solution was injected s.c. in the neck (2 x 5 ml) to prevent dehydration. During the experiment, the animal was kept in a soundproof room. O_2 saturation, heart rate, respiratory rate and CO_2 were monitored during the procedure. Before implanting the DLP printed scaffolds, an acute perforation was made in the left TM of the rabbits with a 23-gauge (G) needle in the posterior part of the *pars tensa* under endoscopic guidance (Hopkins rod 30° endoscope) (Supplementary information S.7., Figure S12). After surgery, the animals were kept under supervision and were placed under a heat lamp until they awoke from anaesthesia. After four weeks, the animals were examined by endoscopy after they were anaesthetized. Afterwards, the animals were euthanized with a pentobarbital (100 mg/kg) injection in the lateral ear vein. The ME bullas were removed and stored at 4°C prior to the *ex vivo* measurements.

2.7. *Ex vivo* evaluation

2.7.1. LDV

Laser doppler vibrometry (LDV) was used to measure the single-point vibration response of the ME components to sound [26]. A loudspeaker was connected via a flexible tube to a closed cavity mounted onto the entrance of the ear canal, which was acoustically sealed using a two-component silicone paste (Dreve Otoplastik GmbH, Otoform Akx, Unna, Germany). The sound pressure level was measured in front of the TM using a probe microphone inserted inside the cavity. To enhance reflectivity of the

laser beam on the sample, a small piece of retroreflective aluminum foil (< 0.04 mg) was attached to the umbo and the footplate. The vibrations of the umbo and footplate were measured with a laser vibrometer (Polytec model OFV-534) coupled to a surgical microscope. During the measurements, the samples were moisturized with an ultrasonic humidifier. Steady-state vibration velocity magnitudes and phases were measured as a function of frequency (100 - 20 000 Hz) under sound pressure loads of 90 dB SPL.

2.7.2. DIC

Digital image correlation (DIC) was used to measure the deformation and corresponding strain field of the TM under quasi-static pressure loads. Details of the experimental procedure can be found in previous work [27,28], but is explained here briefly. The soft ear canal was cut away, exposing the bony ear canal. The bulla was opened, and bone was cut away, giving a medial view on the ME. In this method, the sample was speckled with a stochastic pattern by spraying a suspension of fluorescent powder in ethanol onto the sample. After evaporation, fluorescent particles remained on the surface. The TM was illuminated with a 100 mW green laser beam. Low pass filters were positioned in front of the cameras, so only the orange fluorescence light of the speckle pattern was recorded. The specimens were subjected to quasi-static pressure cycles at low frequencies between 0.01 and 20 Hz using a custom-made pressure generator which was connected to a plastic tube that was glued to the bony ear canal. A single pressure cycle consisted of linearly increasing pressure from 0 kPa to 2 kPa, subsequently decreasing from 2 kPa and returning to 0 kPa. Two cameras installed under a relative angle (~32°) were used to record the deformation of the sample as a function of time. The distance between the camera lens and the TM was ~120 mm. During the measurements, the samples were kept moisturized using an ultrasonic humidifier. The images captured by the cameras were then transferred to the DIC software (Dantec Dynamics, ISTRA 4D, Skovlunde, Denmark) for further stereo correlation to determine the 3D deformation and strain fields of the samples.

2.7.3. Histology

A histological examination was performed to visualize the composition of the tissue. The samples were fixated for approximately 1 week. The samples were then decalcified for 4 to 8 h depending on the size of the sample. After the specimens were embedded in paraffin, 5 µm sections, perpendicular to the umbo, were made on a microtome. Every 500 µm, a section was stained using hematoxylin-eosin (H&E) staining. Eventually, the 1500 µm sections were digitized using a charge-coupled device (CCD) camera connected to an optical microscope.

2.8. Statistical analysis

Quantitative data were analysed by one- or two-way analysis of variance (ANOVA) test with Tukey's multiple comparisons using GraphPad Software v 8.0.2. A value of $p < 0.05$ was considered statistically significant.

3. Results and discussion

3.1. Digital light processing ink optimization

For DLP printing, both the PI and PA should exhibit absorbance around 405 nm, which is the wavelength at which the DLP printer operates. The absorbance spectra of the two PI's (0.1 mg/ml Li-TPO-L and 0.1 mg/ml TPO-L) and tartrazine as PA (0.1 mg/ml) in the two solvents (PBS and NMP) were compared using UV-Vis spectroscopy (Supplementary information S.3.). In the case of tartrazine, the active absorbance is indeed situated in the range of 405 nm when dissolved in both solvents which is consistent with literature [29,30]. When NMP is employed as solvent instead of PBS, the spectrum shifts somewhat. Both PIs absorb light in the visible area from 400 to 420 nm, which is consistent with literature [29,31,32].

Droplet tests (Supplementary information S.4.) enabled to delineate the appropriate printer settings for efficient crosslinking of the various resins. More specifically, both the light intensity (7.26 - 41.3 mW/cm^2) of the printer and the exposure time (3 - 30 s) were varied. A range of different concentrations was chosen for GelMA-based solutions, namely 10, 15, 20, and 30 wt% dissolved in PBS. Gelatin concentrations exceeding 30 wt% result in highly viscous solutions which are not compatible with DLP [33]. Furthermore, a range of PI (Li-TPO-L) concentrations was assessed, including 0.01, 0.1, 1, and 2 wt% to identify the most efficient biocompatible photo-crosslinking of the developed resins [34,35]. The concentration of thiol groups for the GelNBNB and E-PCL solution was chosen to be equimolar with respect to the crosslinkable 'ene' moieties present in GelNBNB and E-PCL. An excess of thiols results in a higher amount of unreacted thiols while a lower amount leads to unreacted 'ene' functionalities, resulting in inefficient network formation and/or biocompatibility issues [34,36]. Table 2 summarizes the range of printing parameters selected based on the results of the droplet tests of GelMA and E-PCL. Based on earlier reported lower PI concentration ranges for gelatin-based thiol-norbornene crosslinking versus GelMA, a tenfold lower PI concentration range was subsequently selected for GelNBNB [37]. For the E-PCL solution, the range of PCL concentrations, namely 50, 60 and 70 wt% dissolved in NMP, was selected based on our previous study [38,39]. A range of different PI (TPO-L) concentrations, namely 0.1, 1, 1.25, and 2.5 wt%, was investigated for the E-PCL resins. The two higher concentrations were also chosen based on previous work [38,39]. The two lower concentrations were chosen to maintain similarity with the range chosen for the gelatins. Based on the findings, a range with the lowest PI concentrations was selected, for which crosslinking was most efficient (Table 2). Specific intensities were chosen for the rheology measurements, which were 19.51 and 29.52 mW/cm^2 for the gelatins and E-PCL, respectively (Table 2). The 50 wt% E-PCL solution required high PI concentrations and long exposure times and was thus excluded from further testing.

Table 2: Overview of the range of printing parameters exploiting the different materials.

	PI range (wt%)	*Light intensity (mW/cm^2)*
GelNBNB	0.01 – 0.1	19.51
GelMA	0.1 - 1	19.51
E-PCL	1.25 - 2.5	29.52

Furthermore, the photo-crosslinkable resin should have a sufficiently low viscosity to allow the resin to flow back. A resin with a viscosity lower than 5 Pa.s at a shear rate of 100/s should be DLP printable [40]. Based on this threshold, the viscosity of the different material solutions was evaluated. First, the viscosity up to 30 wt% GelMA was evaluated at 37°C (Figure 1A). Based on the results, the rheology measurements were continued with 30 wt% GelMA since it has a viscosity value below 5 Pa.s at 100/s and it was hypothesized that it would result in superior mechanical properties in comparison with lower GelMA concentrations. Next, the influence of the addition of PI and PA on the viscosity of the resin was evaluated (Figure 1B and 1C). Both the range of PI (0.1 and 1 wt%) and the range of PA (0.001, 0.01, and 0.1 wt%) did not show a significant influence on the viscosity of 30 wt% GelMA resins. Similar viscosity tests were performed with GelNBNB combined with GelSH as the thiolated crosslinker. To prevent the formation of disulfide bonds, TCEP was added at a concentration of 0.5 eq TCEP with respect to the thiol groups present in the resin. Since the incorporation of PI and PA did not show a substantial impact on the viscosity of the GelMA solutions, the latter was not evaluated for the GelNBNB solutions. The viscosity was evaluated for concentrations up to 20 wt% since the latter exceeded the viscosity threshold compatible with DLP. Therefore, subsequent measurements were performed exploiting 15 wt% GelNBNB (Figure 1D). The viscosity of the E-PCL solutions (60 and 70 wt%) combined with PETA4SH is shown in Figure 1E. Both E-PCL concentrations had a viscosity below the threshold and were thus suitable for DLP printing. Equivalent to what is seen with the GelMA solutions, the addition of PI (TPO-L) and PA had no significant impact on the viscosity of the E-PCL solutions (Figure 1F and 1G).

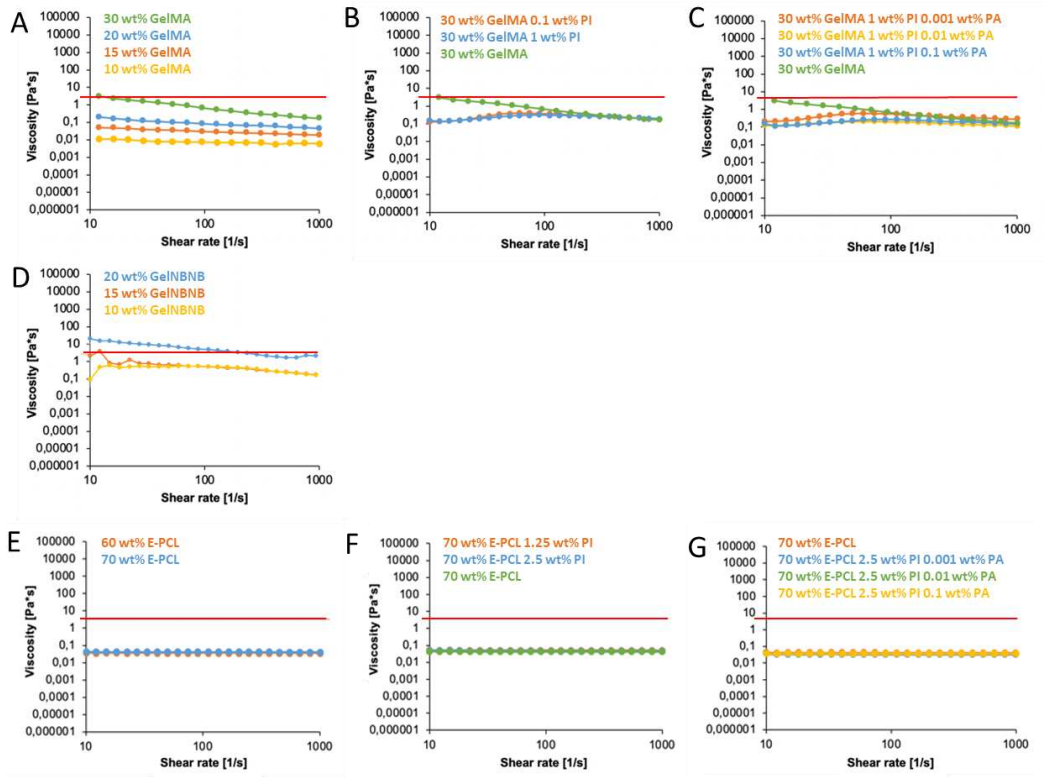

Figure 1: Digital light processing viscosity evaluation: GelMA ink viscosity evaluation for 10, 15, 20 and 30 wt% GelMA with threshold at 5 Pa.s (A), 30 wt% GelMA with no PI, 0.1 and 1 wt% PI with threshold at 5 Pa.s (B), 30 wt% GelMA with no PI or PA, 1 wt% PI with 0.001, 0.01 and 0.1 wt% PA with threshold at 5 Pa.s (C), GelNBNB ink viscosity evaluation for 10, 15, 20 and 30 wt% GelNBNB with threshold at 5 Pa.s (D), E-PCL ink viscosity evaluation for 60 and 70 wt% E-PCL with threshold at 5 Pa.s (E), 70 wt% E-PCL with no PI, 1.25 and 2.5 wt% PI with threshold at 5 Pa.s (F) and 70 wt% E-PCL with no PI or PA versus 2.5 wt% PI with 0.001, 0.01 and 0.1 wt% PA with threshold at 5 Pa.s (G).

To evaluate the photo-curing kinetics of the resins, *in situ* rheological tests were performed combined with UV-light irradiation (Supplementary information S.5.). The crosslinking efficiency was optimal for GelMA upon increasing the PI content to 1 wt%. Secondly, the higher the GelMA concentration, the higher the storage modulus after crosslinking which is consistent with earlier reports in literature [15,35]. To ensure optimal mechanical properties and efficient crosslinking, the evaluation was continued using 30 wt% GelMA combined with 1 wt% PI. Next, the influence of different PA concentrations (0.001, 0.01, 0.1 wt%) on the photo-curing kinetics and mechanical properties was examined and compared to the condition without PA. Overall, the *in situ* photo-rheology results for GelMA showed a minor effect of the PA on either the crosslinking kinetics or the mechanical properties only for the highest concentration of PA (0.1 wt%) (Figure 2A). The difference in mechanical properties of GelNBNB crosslinked with GelSH versus GelMA can be attributed to the lower polymer concentration exploited (15 wt% versus 30 wt%). The evaluation was continued with 0.1 wt% PI for GelNBNB due to the higher storage moduli and optimal crosslinking kinetics. Similar as what was observed for the GelMA resins, only the highest concentration of PA (0.1 wt%) showed a slight impact on the crosslinking kinetics of GelNBNB combined with GelSH (Figure 2B). For E-PCL, faster crosslinking and higher storage moduli were achieved when increasing the PI concentration. For this reason, further examination of E-PCL resins was performed using 2.5 wt% PI. More variation in crosslinking efficiency was seen with increasing PA concentration (Figure 2C). Overall, these findings suggest that increasing the concentration of PA results in a delay in the photocuring reaction, a phenomenon that has also been described earlier in literature [30].

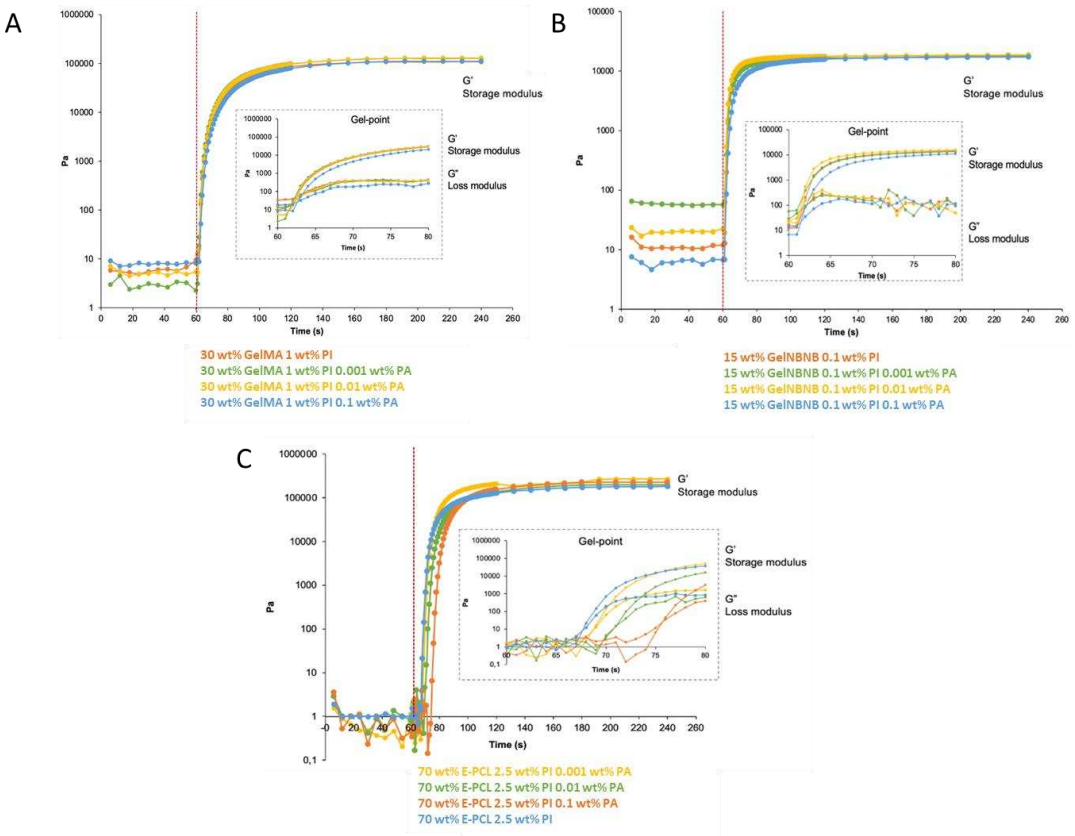

Figure 2: Digital light processing crosslinking efficiency evaluation: *In situ* photo-rheology of 30 wt% GelMA containing 1 wt% PI and 0.001, 0.01 or 0.1 wt% PA, gel-point indicated in inset (A), *In situ* photo-rheology of 15 wt% GelNBNB containing 0.1 wt% PI and 0.001, 0.01 or 0.1 wt% PA, gel-point indicated in inset (B) and *In situ* photo-rheology of 70 wt% E-PCL containing 2.5 wt% PI and 0.001, 0.01 or 0.1 wt% PA, gel-point indicated in inset (C). Onset of UV-A irradiation after 60 s (indicated by red dash line).

To allow high crosslinking efficiency within minimal printing times, the two lowest PA concentrations (0.001, 0.01 wt%) were investigated further in a working curve, in terms of the energy dose required to achieve a certain sample thickness for the three materials. The different resins were cured at a known energy dose. The intensity was kept constant at 19.51 mW/cm^2 for the modified gelatins and 29.52 mW/cm^2 for E-PCL. The applied energy dose was varied by increasing the exposure time. For the gelatin-based resins, there was no effect of increasing the PA concentration above 0.001 wt% and hence this PA concentration was used for further printing optimization. Regarding the E-PCL resin, the PA concentration of 0.01 wt% was chosen given the lower variability of the working curve points compared to the lower PA concentration. Table 3 provides an overview of the chosen resins and their respective characteristics. The *gel-point* or gelation time was determined from the cross-over between the storage and loss moduli (Figure 2) and indicates the transition from predominantly viscous to elastic behaviour. *Time to plateau* was the point where two subsequent values of storage moduli differed less than 10 % from each other. From this timepoint onwards, the final mechanical properties of the crosslinked resin were obtained which is referred to as the *mean plateau value*. GelMA exhibited a lag phase (i.e. a higher gel point) when exposed to UV-light compared to the gelatin-based thiol-ene networks [17]. This lag phase occurred as a result of oxygen inhibition, which did not occur in step-growth thiol-ene systems [41]. Furthermore, the E-PCL resin had a gel-point of 3.58 s, which is consistent with literature (5 s) indicating efficient photo-crosslinking [22]. Both GelMA and E-PCL had higher gel-points and time to plateau which indicated that both GelMA and E-PCL would require longer printing times than the GelNBNB resin. When all three resins are evaluated, a clear range in crosslinking efficiency and mechanical properties is observed.

Table 3: Overview of gel-point, time to plateau and mean plateau value of the different resins.

	15 wt% GelNBNB-GelSH 0.001 wt% PA	*30 wt% GelMA 0.001 wt% PA*	*70 wt% E-PCL 0.01 wt% PA*
Gel-point	0.94 s	1.74 s	3.58 s
Time to plateau	8 s	18 s	26 s
Mean Plateau value	15 kPa	78 kPa	119 kPa

3.2. Digital light processing printing optimization

By using the inks optimized in the previous section, CAD designs of 250 µm (Z-axis) and 10 mm (X-axis) by 10 mm (Y-axis) were printed with a step size of 50 µm. Based on the working curves (Figure 3A-3C), both resins undergoing step-growth photo-crosslinking need shorter printing times than GelMA. These findings are consistent with literature [17]. For E-PCL, the range based on the working curve initially included lower exposure times (5, 6.25, and 7.5 s). However, during printing, the lower two exposure times (5 and 6.25 s) showed poor results for 100 and 150 µm prints. For this reason, the range was expanded with 7.5, 8.75, and 10 s. The printing parameters are summarized in Table 4.

Table 4: Overview of the printing parameters based on the working curves.

	Light intensity	*Range of exposure times (s)*
GelNBNB	19.51 mW/cm^2	5.00
		6.25
		7.50
GelMA	19.51 mW/cm^2	7.50
		8.75
		10.00
E-PCL	29.52 mW/cm^2	7.50
		8.75
		10.00

The resolution of the Z-axis is mainly dependent on the curing depth. Hence, based on the experimental working curve, a range of exposure dosages was evaluated for different sample thicknesses (100, 150, and 200 µm) (X-axis: 10 mm, Y-axis: 10 mm). In case of the GelNBNB and GelMA resin, none of the experimental conditions showed a significant difference from the expected theoretical values (Figure 3D and 3E). Thus, the selection of printing conditions was determined based on the SD values. Since the prints with an energy dosage of 121.94 and 170.71 mJ/cm^2 resulted in the lowest SD values for GelNBNB (103.24 ± 5.56 µm, 150.73 ± 1.64 µm, and 197.36 ± 4.22 µm) and GelMA (104.62 ± 4.97 µm, 151.20 ± 3.19 µm, and 194.33 ± 3.31 µm) respectively, these energy dosages were used as final printing parameters. Based on Figure 3F, the lowest energy dosage, 221.40 mJ/cm^2, for the E-PCL resin was used for further evaluation since none of the experimental values differed significantly from the theoretical values (102.89 ± 7.62 µm, 160.34 ± 4.81 µm, and 224.56 ± 1.50 µm). For the range of exposure times or energy dosages determined through the working curves, a range in XY-dimensions was printed and measured with a caliper (Z-axis: 200 µm). The XY-axis resolution mainly depends on the resolution of the digital mirror device (DMD) which projects the light pattern determined by the CAD design. Based on the theoretical value, there are no significant differences between the experimental and the theoretical values for each resin (Figure 3G-3I). The latter confirmed the selection for the above-mentioned energy dosages for each resin. The final resin compositions and printing parameters for the *in vivo* studies are listed in Table 5. Scaffolds with 100 µm thickness and 4 mm in diameter were prepared for the *in vivo* studies (Figure 3J).

Table 5: Overview of the final resin compositions and their respective printing parameters.

	PI	*PA*	*Exposure time*	*Light intensity*	*Energy dose*
15 wt% GelNBNB	0.1 wt%	0.001 wt%	6.25 s	19.51 mW/cm^2	121.94 mJ/cm^2
30 wt% GelMA	1 wt%	0.001 wt%	8.75 s	19.51 mW/cm^2	170.71 mJ/cm^2
70 wt% E-PCL	2.5 wt%	0.01 wt%	7.50 s	29.52 mW/cm^2	221.40 mJ/cm^2

For further optimization of the materials for DLP printing, porous scaffolds were printed (Figure 3K). The scaffolds were 200 µm thick and constituted of pores and struts of 1000 µm and 400 µm respectively. These dimensions were chosen to provide a first indication regarding the ability of the optimized resins to form pores within the scaffolds. To achieve actual pores with the GelMA resin, a higher concentration of PA was needed (0.1 wt%). GelNBNB and E-PCL had the same composition as previously described (Table 5).

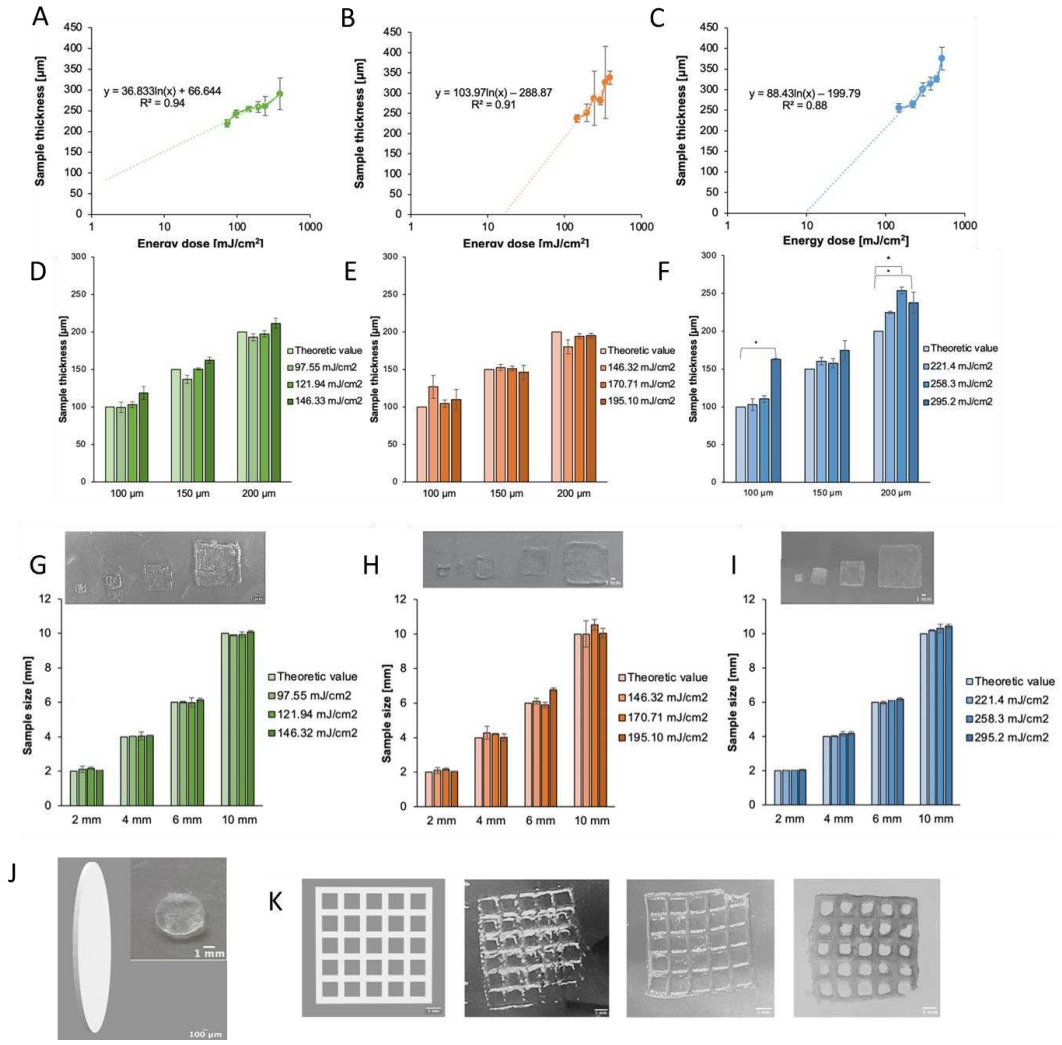

Figure 3: Digital light processing print optimization: Working curve for 15 wt% GelNBNB containing 0.001 wt% PA printed at 19.51 mW/cm^2 (A), Working curve for 30 wt% GelMA containing 0.001 wt% PA printed at 19.51 mW/cm^2 (B), Working curve for 70 wt% E-PCL containing 0.01 wt% PA printed at 29.52 mW/cm^2 (C), Z-axis optimization for GelNBNB (D), GelMA (E), E-PCL (F), XY-axis optimization (scale bar = 1 mm) for GelNBNB (G), GelMA (H), E-PCL (I), *In vivo* CAD design with thickness of 100 µm (scale bar = 100 µm), inset showing DLP printed 30 wt% GelMA scaffold, containing 1 wt% PI and 0.001 wt% PA (scale bar = 1 mm) (J) and Porous scaffold CAD design (strut size = 400 µm and pore size = 1 mm) and GelNBNB, GelMA and E-PCL prints with measured pore and strut sizes (scale bar = 1 mm) (K). Two-way ANOVA was used to evaluate statistical significance (*). Error bars represent the standard deviation.

3.3. Physico-chemical and *in vitro* testing

The gel fraction represents the remaining mass fraction of the photo-crosslinked polymer after leaching out of the non-crosslinked parts of the network. Because leaching out of material can be harmful to an organism, obtaining a high gel fraction is critical to reduce the risk of potentially toxic precursors leaching out [42]. Furthermore, a high gel fraction indicates an efficiently crosslinked network. Both the GelNBNB (95.4 ± 3.5 %) and E-PCL (98.2 ± 0.6 %) prints exhibited high gel fractions which indicates excellent network integrity and thus efficient crosslinking (Figure 4A). This is especially clear when compared to the GelMA prints, which had a lower gel fraction (72.2 ± 7.6 %). The main difference with the GelMA print is the chain- versus step-growth polymerization and the results are in accordance with literature [17,42]. The lower GelMA gel fraction underlined the need for a post-curing step following printing.

The swelling degree (Figure 4B) of the prints was quantified since swelling of the hydrogel can result in deviations from the applied CAD design following printing potentially impacting the mechanical properties. The GelMA prints (76.3 ± 6.5 %) were characterized by a lower mass swelling degree in comparison to the GelNBNB prints (90.3 ± 1.3 %). This can be explained by the presence of hydrophobic kinetic oligo-methacrylamide chains within the GelMA network [17]. In addition, the GelNBNB prints have a more homogeneous network topology due to the step-growth polymerized thiol-ene networks while the chain-growth polymerization results in a more densely crosslinked heterogenous network [43]. The E-PCL prints had the lowest swelling degree (39.6 ± 9.6 %). This can be explained by the hydrophobic nature of PCL. Furthermore, a trend is seen that an increase in polymer concentration corresponds to a lower swelling degree, in line with expectations since a higher concentration results in a denser network formation.

To further evaluate the influence of the crosslinking efficiency (measured through the gel fraction) and the swelling effect (measured through the swelling degree) on the presented mechanical properties, frequency sweep testing on chemically crosslinked, equilibrium swollen sheets was applied (Figure 4C). Similarly as the storage modulus reported earlier in the *in-situ* photo-rheology section, the crosslinked E-PCL network exhibited the highest storage modulus (124 kPa). Despite the high gel fraction of the GelNBNB hydrogels, the equilibrium swollen and chemically crosslinked GelMA network nevertheless outperformed (63 kPa for GelMA versus 46 kPa for GelNBNB) its thiol-ene counterpart in terms of the presented mechanical properties thanks to the higher concentration that could be applied with GelMA leading to more available photo-crosslinkable moieties and hence a more densely crosslinked network with a reduced swelling degree. Overall, a distinctive mechanical range could be presented which was further evaluated for its *in vitro* and *in vivo* response.

A live/dead assay was performed before the start of the *in vivo* studies to evaluate potential fibroblast cytotoxicity since this is the main cell type involved in the regeneration of the collagen fiber network in the native connective tissue (Figure 4D and Supplementary information S.6.). The samples for *in vitro* evaluation included a 30 wt% GelMA printed construct (1 wt% PI and 0.001 wt% PA), a 15 wt% GelNBNB printed construct (0.1 wt% PI, 0.001 wt% PA and 0.5 eq TCEP), a 70 wt% E-PCL printed construct (2.5 wt% PI and 0.01 wt% PA), while tissue culture plastic (TCP) was used as a positive control (non-toxic). The indirect cell test results showed that the overall viability of the human foreskin fibroblasts (HFF) on days 1, 14 and 28 exceeded 93 %. These results illustrated that the scaffolds are highly biocompatible since the threshold is set at 70 % (according to ISO 10993-5:2009).

An MTS assay was performed to evaluate the metabolic activity of the fibroblasts. Cell metabolic activity was evaluated at days 1, 14 and 28 (Figure 4E). The metabolic activity of the cells in the three groups, GelNBNB, GelMA, and E-PCL was 97.84 ± 0.2 %, 99.31 ± 0.05 %, 101.84 ± 0.07 % relative to TCP, respectively on day 28. When compared to days 1 and 14, the activity was the highest on day 28. In the GelMA and E-PCL group, a slightly increasing trend in metabolic activity was seen, while for the

GelNBNB group, the activity on day 14 was lower compared to days 1 and 28. Overall, the results showed that the metabolic activity, which can give an indication of cell proliferation but also of cellular stress, is above 88 %. Thus, the MTS assay results were in line with the results from the live/dead assay, hence indicating that the high MTS values can be attributed to a higher cell proliferation. Both the results of the live/dead and MTS assay are in accordance with literature [39,42]. Since both *in vitro* assays showed good cell viability and metabolic activity, the GelNBNB, GelMA and E-PCL scaffolds were considered biocompatible until day 28. Therefore, all three scaffolds were included in the *in vivo* evaluations.

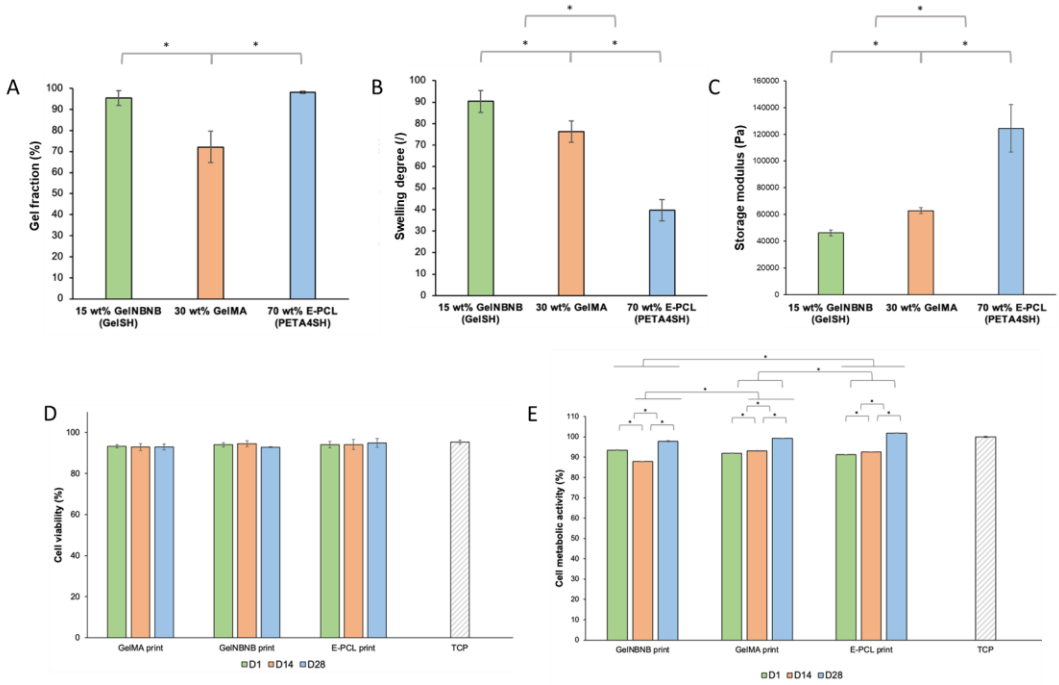

Figure 4: Physico-chemical and *in vitro* testing: Gel fraction of GelMA, GelNBNB and E-PCL prints (A), Swelling degree of GelMA, GelNBNB and E-PCL prints (B), Frequency sweep storage moduli of crosslinked disks after equilibrium swelling at 37°C (C), Indirect fibroblast viability quantification at D1, D14 and D28 with TCP as reference (D) and Indirect fibroblast metabolic activity quantification at D1, D14 and D28 with TCP as reference (E). One-way ANOVA was used to evaluate statistical significance of the performed physico-chemical testing whereas two-way ANOVA was used to evaluate statistical significance of the performed *in vitro* testing (*). Error bars represent the standard deviation.

3.4. *In vivo* testing

The use of rabbits as an animal model for this application is exploited since it is a mammalian model whose hearing range is comparable to that of humans and extends to relatively low frequencies [44,45]. The species selection is also based on its similarity to the anatomy of the human ME and its size (Figure 5A) [46]. The different *in vivo* conditions and their accompanying codes (HC = healthy control, PC = perforated control) are shown in Table 6. After four weeks, both the experimental and control TMs were visualized through an endoscope (Supplementary information S.7., Figure S13).

Table 6: Overview of the different *in vivo* conditions and their accompanying codes.

	GelNBNB			***GelMA***			***E-PCL***		
	K8	K2	K4	K12	K3	K14	K11	K9	K6
Left	Sample	Sample	Sample	Sample	Sample	Sample	Sample	Sample	Sample
Right	HC	PC	PC	HC	PC	PC	HC	PC	PC

Before performing the LDV measurements, images were taken of each sample except for two healthy control samples, namely K8R and K11R. In the case of the GelNBNB condition (Supplementary information S.7., Figure S14), two samples had a perforation, and one was healed, while the two perforated controls both showed a visually healed TM. There was a clear difference in the size of perforation between the two perforated TMs. In the case of the GelMA implanted TMs (Supplementary information S.7., Figure S15), two TMs appeared healed while one had a clear perforation. The perforated control conditions both showed visually healed TMs. Lastly, all the TMs which were implanted with a E-PCL scaffold had a healed TM (Supplementary information S.7., Figure S16). Both perforated controls and all three scaffold conditions appeared to be healed.

Laser doppler vibrometry (LDV) was used as a first non-contact optical methodology to study the physiological vibration of the tympanic membrane. The transmission characteristics of the ME can be determined by measuring the movement of stapedial footplate or the umbo at a known sound pressure [47]. A clear range of vibration response values was seen for the visually healed perforated controls (Figure 5B), which might also possibly explain part of the variability in vibration response for the implanted TMs (Figure 5C-5E). Due to this, the implanted TMs which were situated within the healthy and healed perforated control range, were more difficult to evaluate since this could be just due to the normal variability. However, in case the response was below this range, it could suggest the results were substandard. First, in the GelNBNB experimental group (Figure 5C), the healed sample (K2L) provided a similar vibration response as the healthy control sample. The other two samples, K8L and K4L, were both perforated and had an expected lower response. One of the visually regenerated perforated controls, K2R, had a lower response than both the healthy control (K8R), the healed implanted sample (K2L) and the other regenerated perforated control (K4R). Furthermore, sample K8L gave a lower response than K4L since K8L had a larger perforation compared to K4L. Secondly, in the GelMA experimental group (Figure 5D), both healed samples, K12L and K3L, showed a good vibration response. Moreover, in comparison, K3L showed a better response since it was closer to the healthy control and had a higher resonance peak. The perforated sample, K14L, had the lowest response, which was similar to the visually regenerated perforated control, K2R. The other two visually regenerated perforated controls, K3R and K14R, gave a similar response as the healthy control, K12R. Lastly, in the E-PCL experimental group (Figure 5E), sample K9L clearly gave a substandard response. Moreover, based on the umbo velocity phase information, sample K9L had a phase shift correlating to a resonance peak at a higher frequency than the other samples. This is often seen in samples that are dehydrated resulting in stiffer tissue [27]. The sample was rehydrated to rule out dehydration, and the same results were obtained, thus indicating that this sample could be stiffer than the other samples. Furthermore, K6L gave a response just below the two visually regenerated perforated controls (K9R and K6R). However, these control samples were situated more at the lower perforated control range (Figure 5B), thus sample K6L could be considered substandard. The third sample of E-PCL is not included since this sample had a broken malleus and could thus not provide a relevant vibration response (Supplementary information S.7., Figure S17). Sample K11R got perforated during dissection and was therefore left out of the evaluation.

As a second functional characterization, digital image correlation (DIC) was used to measure the deformation and corresponding strain field in the material under quasi-static pressure loads between ± 2 kPa. Over- or positive pressure in the ear canal results in the medial or positive displacement of the umbo which is normally smaller than the lateral or negative displacement as the result of under- or negative pressure [27]. Due to the viscoelastic behaviour of the TM and the ME mechanical system, the analysis was performed after two preconditioning cycles so repeatable displacement curves were obtained. For the DIC measurements, only one healthy sample was included as reference. Also, only the samples which were healed and had an intact malleus were included (Supplementary information S.7., Figure S18). The samples K11R and K6R were excluded because the samples got damaged during dissection. First, in the GelNBNB experimental group, only one implanted TM, K2L, was healed. However, in comparison to the control results, a clear region of strain was visible (Figure 5F). The

results of the visually spontaneously regenerated controls also showed a similar region of strain. This could indicate that the samples were not fully healed yet after four weeks. In the case of K4R, the under-pressure was also evaluated and showed more compression (Figure 5G). Thus, the tissue was not completely inverted at under-pressure (-2kPa). For sample K2R, after examination of the under-pressure images, it became clear this sample contained two small perforations (Supplementary information S.7., Figure S19). It was not clear whether these perforations resulted from the pressure cycles or if they were already present. Secondly, in the GelMA experimental group, two of the implanted TMs were healed. Similar to what was seen in the GelNBNB sample, clear regions of strain were visible in the implanted TMs (Figure 5F and Supplementary information S.7., Figure S18). However, both visually spontaneous regenerated samples K3R and K14R showed similar strain as the control sample K8R. Lastly, in the E-PCL experimental group, K9L was imaged at time point 8 since the image at point 50 did not provide a lot of information (Supplementary information S.7., Figure S20). When the movement of the TM under the quasi-static pressure fluctuations was studied, it seemed that there was an unperforated region that showed irregular movements which probably caused the data shortage at timepoint 50. This region was also seen on the microscopy images (Supplementary information S.7., Figure S16). Furthermore, samples K6L and K9R also showed a clear region of strain indicating the perforation was not fully healed (Figure 5F and Supplementary information S.7., Figure S18). When this was compared to images at under-pressure (Figure 5G), the K9R sample showed compression and was not fully inverted yet. Sample K6L showed both a strain and compression response and showed a pattern that was more comparable to the control (Figure 5G). When compared to the microscopy image of K6L, the strain and compression were located at the white spot (Supplementary information S.7., Figure S16). At this region, the TM showed a wrinkly pattern during the pressure cycles indicating the previously perforated area.

When the total displacement of samples K4R and K3L was compared to their strain pattern, it became clear that the total displacement is not always easy to interpret (Supplementary information S.7., Figure S21). In the case of sample K4R, the highest displacement was seen in the region of high strain, while for sample K3L, the region of high displacement did not necessarily correlate to the high strain region. Thus, a region of high total displacement does not necessarily correspond to a region of high strain. The hypothesis is that due to a bigger strain region, the other more homogenous regions are not able to move as much since the bigger strain region is more flexible, thus resulting in a less representable displacement pattern caused by over- and under-pressure. Therefore, net displacement of the different samples was further evaluated at the umbo (Supplementary information S.7., Figures S22-S25). The ratio of the displacement at the upper and lower limit of pressure was for all samples between 0.6 and 1.4 including four (K12L, K14R, K9R and K6L) out of eleven samples having a ratio of 1. This means that the displacement pattern for these samples was symmetrical. Furthermore, four (K2R, K4R, K3L and K3R) samples of the remaining seven samples had an asymmetrical displacement ratio (0.75, 0.6, 0.86, and 0.83) with the medial being bigger than the lateral, which is opposite to what is normally seen [27]. The remaining three samples (K8R, K2L and K9L) had an asymmetrical displacement with the ratio being 1.2, 1.25, and 1.4 respectively.

The histological H&E staining is shown in Figure 5H. The implanted sample K2L and the regenerated control K9R showed a perforation that was not present during the earlier measurements hence indicating that the tissue was not fully healed yet and was hence too delicate for histological manipulation. When the control was compared to the remaining samples, a similar detailed image was observed for sample K9L. However, the detailed image of the rest of the samples showed a thicker layer of tissue compared to the control. Since the histological qualification images only 5 μm of the entire tissue, it is difficult to draw conclusions solely based on these images. On the other hand, the thicker tissue region could indicate a region with a lot of cell activity indicating that the tissue was not fully healed yet which correlates with the earlier microscopy results [48]. Table 7 gives an overview of the different *in vivo* conditions, their accompanying codes and their outcome according to the morphological and functional tests performed.

Table 7: Overview of the different *in vivo* conditions, their accompanying codes and their outcome according to the morphological and functional tests performed (in the following order: microscopy after dissection | LDV | DIC | histology, with green indicating an outcome comparable to included healed controls, orange a suboptimal outcome and grey when the test was not conducted for the specific sample).

	GelNBNB			***GelMA***			***E-PCL***		
	K8	K2	K4	K12	K3	K14	K11	K9	K6
Left	Sample	Sample	Sample	Sample	Sample	Sample	Sample	Sample	Sample
Right	HC	PC	PC	HC	PC	PC	HC	PC	PC

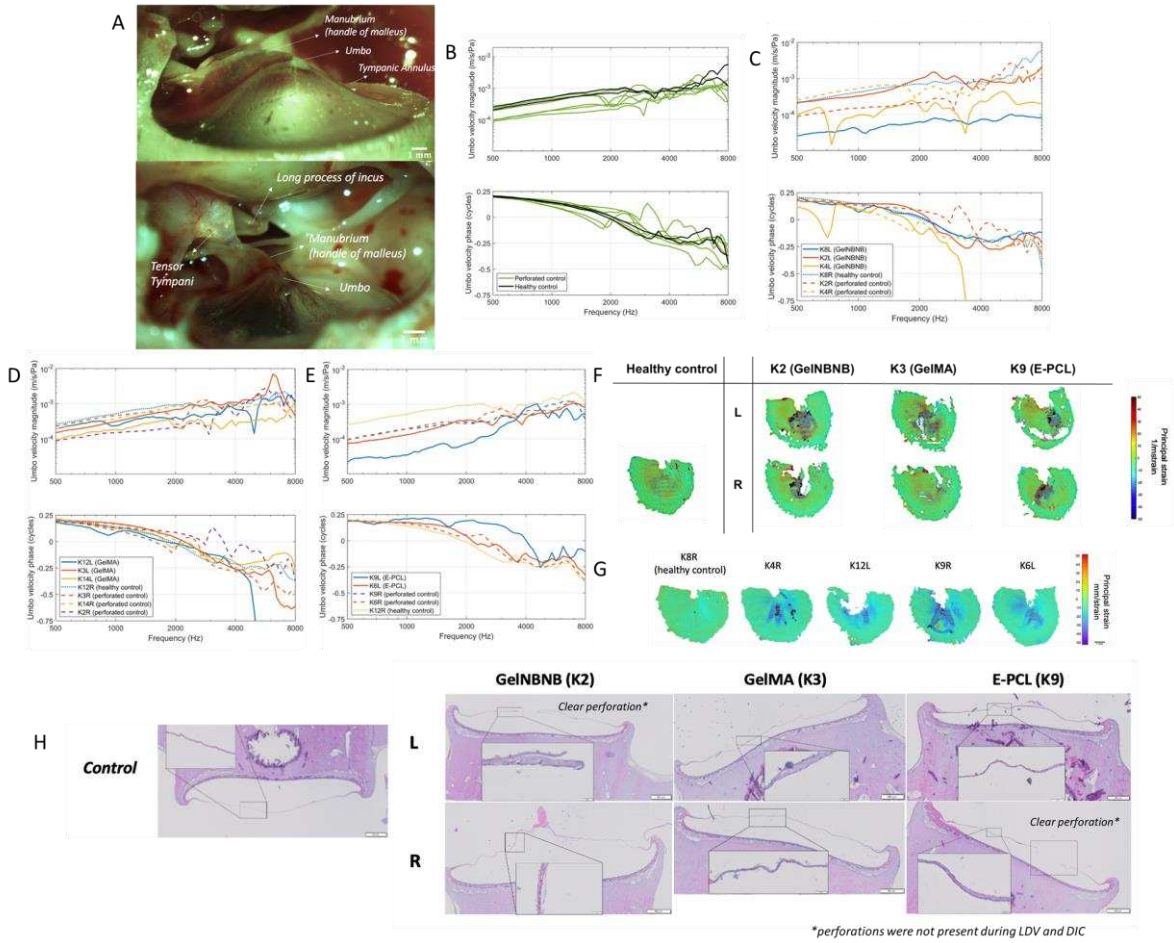

Figure 5: *Ex vivo* evaluation of the implanted TM study: Images taken with a surgical microscope of sample K14R (Scale bar = 1 mm) (A), LDV plots with an overview of velocity magnitude (m/s/Pa) and phase (cycles) response of all control samples including the visually healed perforated controls and healthy controls (B), LDV plots of the GelNBNB experimental group, a healthy control, and regenerated perforated controls (C), LDV plots of the GelMA experimental group, a healthy control, and regenerated perforated controls (D), LDV plots of the E-PCL experimental group, a healthy control, and regenerated perforated controls (E), DIC measurements showing the principal strain of the healthy control (K8R) and the left and right samples in the GelNBNB experimental group (K2), the GelMA experimental group (K3) and the E-PCL experimental group (K9) (Strain magnitude is represented by color correlating to the color scale. Scale bar = 1 mm) (F), Images of specific samples at under-pressure (timepoint 60) of -2kPa (Strain magnitude is represented by color correlating to the color scale. Scale bar = 1 mm) (G) and H&E staining of controls (non-perforated K8R, perforated K2R, K3R and K9R samples) and experimental TMs (GelNBNB K2L sample, GelMA K3L sample and E-PCL K9L sample) (H) (1.6x magnification and scale bar of 500 µm, inset 40x magnification and scale bar of 20 µm).

4. Conclusion and future perspectives

Photo-crosslinkable materials, namely GelMA, GelNBNB, and E-PCL were developed and combined with a PI to develop a DLP printable resin. Due to the step-growth polymerization process of GelNBNB and E-PCL, these materials were also combined with a thiolated crosslinker. The characterization and optimization of the photo-crosslinkable materials led to the development of three printing inks with specific material, PI and PA concentrations. These final inks were characterized by different curing kinetics and mechanical properties. All developed inks had a gel-point within +/- 4 seconds, indicating excellent crosslinking kinetics. Moreover, the various final resins exhibited a range of mechanical properties, allowing to study the impact of these properties on the printing process itself, the cellular response, and *in vivo* studies. The working curves generated in this work provided a first indication of the most efficient printing parameters. After fine-tuning the Z- and XY-axis resolution, thin and porous scaffolds were printed. Although the use of TCEP excluded disulfide formation, it would be interesting in forthcoming research to focus on the development of stable GelNBNB-GelSH inks with a higher concentration and superior mechanical properties while enabling DLP printing. Furthermore, the mechanical properties of the GelMA ink in this work were at their limit due to the viscosity of the resin. In forthcoming research, it could be interesting to work with gelatin-methacryloyl-aminoethyl-methacrylate (GelMA-AEMA) inks, which are characterized by superior mechanical properties [49]. The increase of the mechanical properties of GelMA-AEMA compared to GelMA is achieved by introducing additional crosslinkable moieties through partial modification of the carboxylic acids of glutamic and aspartic acid. Finally, the E-PCL ink was characterized by good crosslinking kinetics and the greatest mechanical properties, which resulted in the most efficient printing process. Forthcoming research should include a further optimization of the inner design of the construct which may evoke the need for a higher resolution printing method such as two-photon polymerization (2PP) which could more accurately enable the development of this more advanced scaffold thanks to its characteristic spatial resolution situated in the sub-micrometer range [36].

Moreover, physico-chemical tests were performed, where the swelling tests revealed that the GelNBNB scaffolds had the highest swelling degree, while E-PCL had the lowest, which can be related to the difference in material concentration and the hydrophobic nature of PCL. In particular, a higher material concentration correlated with a denser network and thus a lower swelling capacity. In forthcoming research, it would be interesting to develop a GelNBNB ink with a higher concentration, not only to achieve superior mechanical properties but also to reduce the degree of swelling. Comparing the gel fraction results, all step-growth inks showed relatively high crosslinking efficiency whereas an extra post-crosslinking step was needed for GelMA. Next, the biocompatibility of the printed scaffolds was evaluated. Both *in vitro* assays, including a live/dead and MTS assay, showed excellent cell viability (> 93%) and metabolic activity (> 88%). The GelNBNB, GelMA, and E-PCL scaffolds were considered biocompatible up to day 28. In future work, it would be interesting to include a co-culture of fibroblasts and keratinocytes which both reside within the TM [50]. This would provide an improved indication of the biocompatibility of potential scaffolds to serve TM regeneration. Furthermore, direct cell tests could be performed to directly test the interaction of cells with the optimized scaffolds. Overall, it can be stated that all networks showed excellent photo-reactivity and crosslinking kinetics, resulting in complete crosslinking within a few seconds leading to excellent cell biocompatibility.

Next, the printed scaffolds were evaluated *in vivo* and *ex vivo*. To investigate the effects of the optimized DLP-printed scaffolds, the scaffolds were implanted into animals with artificially created acute perforations. A high degree of variation in both anatomical and functional evaluations was observed. Yet, there was a first microscopic morphological indication that tissue healing was greatly influenced by the presented mechanical properties, with the most efficient healing observed for the E-PCL scaffolds. Functional studies (LDV, DIC) on the other hand indicated a better quality of the regenerated tissue when cell-interactive domains were present inherent to gelatin-based scaffolds.

Therefore, future work should look into hybrid scaffolds whereby cell-interactivity is combined with superior mechanical properties. To investigate the effects of the scaffolds more accurately, larger animal studies using a chronic perforation model are needed. In addition, more extensive *ex vivo* testing may provide a more thorough overview of the effects of the presented scaffolds.

Acknowledgements

LP, PL and QT would like to acknowledge the financial support from the Research Foundation Flanders (FWO) (1S44221N, 1273723N and 1SA2321N respectively). DV acknowledges the financial support from the Young Universities for the Future of Europe (YUFE). VVR receives a senior clinical investigator fund 18E2524N from FWO.

Declaration of interests

The authors declare that they have no known competing financial interests or personal relationships that could have appeared to influence the work reported in this paper.

Data availability

The datasets generated during and/or analyzed during the current study are available from the corresponding author on reasonable request.

References

[1] G. Volandri, F. Di Puccio, P. Forte, C. Carmignani, Biomechanics of the tympanic membrane, J Biomech. 44 (2011) 1219–1236.

[2] C. Mota, S. Danti, D. D'Alessandro, L. Trombi, C. Ricci, D. Puppi, D. Dinucci, M. Milazzo, C. Stefanini, F. Chiellini, Multiscale fabrication of biomimetic scaffolds for tympanic membrane tissue engineering, Biofabrication. 7 (2015) 025005.

[3] N.P. Daphalapurkar, C. Dai, R.Z. Gan, H. Lu, Characterization of the linearly viscoelastic behavior of human tympanic membrane by nanoindentation, J Mech Behav Biomed Mater. 2 (2009) 82–92.

[4] R. Mittal, C. V Lisi, R. Gerring, J. Mittal, K. Mathee, G. Narasimhan, R.K. Azad, Q. Yao, M. Grati, D. Yan, Current concepts in the pathogenesis and treatment of chronic suppurative otitis media, J Med Microbiol. 64 (2015) 1103.

[5] L. Monasta, L. Ronfani, F. Marchetti, M. Montico, L. Vecchi Brumatti, A. Bavcar, D. Grasso, C. Barbiero, G. Tamburlini, Burden of disease caused by otitis media: systematic review and global estimates, PLoS One. 7 (2012) e36226.

[6] J. Kim, S.W. Kim, S.J. Choi, K.T. Lim, J. Bin Lee, H. Seonwoo, P.-H. Choung, K. Park, C.-S. Cho, Y.-H. Choung, A healing method of tympanic membrane perforations using three-dimensional porous chitosan scaffolds, Tissue Eng Part A. 17 (2011) 2763–2772.

[7] F.T. Orji, C.C. Agu, Determinants of spontaneous healing in traumatic perforations of the tympanic membrane, Clinical Otolaryngology. 33 (2008) 420–426.

[8] E.D. Kozin, N.L. Black, J.T. Cheng, M.J. Cotler, M.J. McKenna, D.J. Lee, J.A. Lewis, J.J. Rosowski, A.K. Remenschneider, Design, fabrication, and in vitro testing of novel three-dimensionally printed tympanic membrane grafts, Hear Res. 340 (2016) 191–203.

[9] J. Caremans, E. Hamans, L. Muylle, P. Van de Heyning, V. Van Rompaey, Endoscopic procurement of allograft tympano-ossicular systems: valuable to replace the Schuknecht bone plug technique?, Cell Tissue Bank. 16 (2015) 91–96.

[10] V. Van Rompaey, J. Caremans, E. Hamans, L. Muylle, P. Van de Heyning, Endoscopic procurement of tympano-ossicular allografts: alternative to the transcranial or retroauricular technique, Cell Tissue Bank. 14 (2013) 511–514.

[11] J. Fay, S. Puria, W.F. Decraemer, C. Steele, Three approaches for estimating the elastic modulus of the tympanic membrane, J Biomech. 38 (2005) 1807–1815.
[12] H. Quan, T. Zhang, H. Xu, S. Luo, J. Nie, X. Zhu, Photo-curing 3D printing technique and its challenges, Bioact Mater. 5 (2020) 110–115.
[13] T. Cheng, C. Dai, R.Z. Gan, Viscoelastic properties of human tympanic membrane, Ann Biomed Eng. 35 (2007) 305–314.
[14] J. Aernouts, J.R.M. Aerts, J.J.J. Dirckx, Mechanical properties of human tympanic membrane in the quasi-static regime from in situ point indentation measurements, Hear Res. 290 (2012) 45–54.
[15] J. Van Hoorick, L. Tytgat, A. Dobos, H. Ottevaere, J. Van Erps, H. Thienpont, A. Ovsianikov, P. Dubruel, S. Van Vlierberghe, (Photo-) crosslinkable gelatin derivatives for biofabrication applications, Acta Biomater. 97 (2019) 46–73.
[16] E. Hoch, C. Schuh, T. Hirth, G.E.M. Tovar, K. Borchers, Stiff gelatin hydrogels can be photo-chemically synthesized from low viscous gelatin solutions using molecularly functionalized gelatin with a high degree of methacrylation, J Mater Sci Mater Med. 23 (2012) 2607–2617.
[17] J. Van Hoorick, A. Dobos, M. Markovic, T. Gheysens, L. Van Damme, P. Gruber, L. Tytgat, J. Van Erps, H. Thienpont, P. Dubruel, Thiol-norbornene gelatin hydrogels: Influence of thiolated crosslinker on network properties and high definition 3D printing, Biofabrication. 13 (2020) 15017.
[18] J. Van Hoorick, P. Gruber, M. Markovic, M. Rollot, G. Graulus, M. Vagenende, M. Tromayer, J. Van Erps, H. Thienpont, J.C. Martins, Highly reactive thiol-norbornene photo-click hydrogels: Toward improved processability, Macromol Rapid Commun. 39 (2018) 1800181.
[19] K. Van de Velde, P. Kiekens, Biopolymers: overview of several properties and consequences on their applications, Polym Test. 21 (2002) 433–442.
[20] M. Vert, S.M. Li, G. Spenlehauer, P. Guérin, Bioresorbability and biocompatibility of aliphatic polyesters, J Mater Sci Mater Med. 3 (1992) 432–446.
[21] M.A. Woodruff, D.W. Hutmacher, The return of a forgotten polymer—Polycaprolactone in the 21st century, Prog Polym Sci. 35 (2010) 1217–1256.
[22] Q. Thijssen, K. Cornelis, R. Alkaissy, J. Locs, L. Van Damme, D. Schaubroeck, R. Willaert, S. Snelling, P.-A. Mouthuy, S. Van Vlierberghe, Tough photo-cross-linked PCL-hydroxyapatite composites for bone tissue engineering, Biomacromolecules. 23 (2022) 1366–1375.
[23] Q. Thijssen, A. Quaak, J. Toombs, E. De Vlieghere, L. Parmentier, H. Taylor, S. Van Vlierberghe, Volumetric printing of thiol-ene photo-cross-linkable poly (ε-caprolactone): a tunable material platform serving biomedical applications, Advanced Materials. (2023) 2210136.
[24] A.I. Van Den Bulcke, B. Bogdanov, N. De Rooze, E.H. Schacht, M. Cornelissen, H. Berghmans, Structural and rheological properties of methacrylamide modified gelatin hydrogels, Biomacromolecules. 1 (2000) 31–38.
[25] S. Van Vlierberghe, E. Schacht, P. Dubruel, Reversible gelatin-based hydrogels: finetuning of material properties, Eur Polym J. 47 (2011) 1039–1047.
[26] J. Peacock, R. Pintelon, J. Dirckx, Nonlinear vibration response measured at umbo and stapes in the rabbit middle ear, Journal of the Association for Research in Otolaryngology. 16 (2015) 569–580.
[27] K. Gladiné, J.J.J. Dirckx, Strain distribution in rabbit eardrums under static pressure, Hear Res. 381 (2019) 107772.
[28] P. Livens, P.G.G. Muyshondt, J.J.J. Dirckx, Prestrain in the rabbit eardrum measured by digital image correlation and micro-incisions, Hear Res. 412 (2021) 108392.
[29] B. Grigoryan, S.J. Paulsen, D.C. Corbett, D.W. Sazer, C.L. Fortin, A.J. Zaita, P.T. Greenfield, N.J. Calafat, J.P. Gounley, A.H. Ta, Multivascular networks and functional intravascular topologies within biocompatible hydrogels, Science (1979). 364 (2019) 458–464.
[30] Y. Yang, Y. Zhou, X. Lin, Q. Yang, G. Yang, Printability of external and internal structures based on digital light processing 3D printing technique, Pharmaceutics. 12 (2020) 207.

[31] B.D. Fairbanks, M.P. Schwartz, C.N. Bowman, K.S. Anseth, Photoinitiated polymerization of PEG-diacrylate with lithium phenyl-2, 4, 6-trimethylbenzoylphosphinate: polymerization rate and cytocompatibility, Biomaterials. 30 (2009) 6702–6707.
[32] B. Rongxia, L. Shiyong, X. Wencai, M. Ruiqiang, H. Di, M. Kelin, H. Jiangwei, X. Yong, L. Caichang, Characterization of the UV-visible absorption spectra of commonly used photoinitiators, J. Syst. Control Eng. 1 (2017) 18–20.
[33] N.G. Parker, M.J.W. Povey, Ultrasonic study of the gelation of gelatin: Phase diagram, hysteresis and kinetics, Food Hydrocoll. 26 (2012) 99–107.
[34] C. Yu, J. Schimelman, P. Wang, K.L. Miller, X. Ma, S. You, J. Guan, B. Sun, W. Zhu, S. Chen, Photopolymerizable biomaterials and light-based 3D printing strategies for biomedical applications, Chem Rev. 120 (2020) 10695–10743.
[35] K. Wang, B. Li, K. Ni, Z. Wang, Optimal photoinitiator concentration for light-cured dental resins, Polym Test. 94 (2021) 107039.
[36] A. Dobos, J. Van Hoorick, W. Steiger, P. Gruber, M. Markovic, O.G. Andriotis, A. Rohatschek, P. Dubruel, P.J. Thurner, S. Van Vlierberghe, Thiol–gelatin–norbornene bioink for laser-based high-definition bioprinting, Adv Healthc Mater. 9 (2020) 1900752.
[37] T. Göckler, S. Haase, X. Kempter, R. Pfister, B.R. Maciel, A. Grimm, T. Molitor, N. Willenbacher, U. Schepers, Tuning Superfast Curing Thiol-Norbornene-Functionalized Gelatin Hydrogels for 3D Bioprinting, Adv Healthc Mater. 10 (2021) 2100206.
[38] A. Quaak, Q. Thijssen, S. Van Vlierberghe, Exploiting the network architecture of thiol–ene photo-crosslinked poly (ε-caprolactone) towards tailorable materials for light-based 3D-printing, Polym Chem. (2023).
[39] Q. Thijssen, L. Parmentier, E. Augustyniak, P. Mouthuy, S. Van Vlierberghe, From chain growth to step growth polymerization of photoreactive poly-ε-caprolactone: the network topology of bioresorbable networks as tool in tissue engineering, Adv Funct Mater. 32 (2022) 2108869.
[40] D.M. Shah, J. Morris, T.A. Plaisted, A. V Amirkhizi, C.J. Hansen, Highly filled resins for DLP-based printing of low density, high modulus materials, Addit Manuf. 37 (2021) 101736.
[41] C.E. Hoyle, C.N. Bowman, Thiol–ene click chemistry, Angewandte Chemie International Edition. 49 (2010) 1540–1573.
[42] L. Van Damme, J. Van Hoorick, P. Blondeel, S. Van Vlierberghe, Toward Adipose Tissue Engineering Using Thiol-Norbornene Photo-Crosslinkable Gelatin Hydrogels, Biomacromolecules. 22 (2021) 2408–2418.
[43] L. Tytgat, L. Van Damme, J. Van Hoorick, H. Declercq, H. Thienpont, H. Ottevaere, P. Blondeel, P. Dubruel, S. Van Vlierberghe, Additive manufacturing of photo-crosslinked gelatin scaffolds for adipose tissue engineering, Acta Biomater. 94 (2019) 340–350.
[44] H. Haragopal, R. Dorkoski, H.M. Johnson, M.A. Berryman, S. Tanda, M.L. Day, Paired measurements of cochlear function and hair cell count in Dutch-belted rabbits with noise-induced hearing loss, Hear Res. 385 (2020) 107845.
[45] M. Stieve, H.J. Hedrich, R.D. Battmer, P. Behrens, P. Müller, T. Lenarz, Experimental middle ear surgery in rabbits: a new approach for reconstructing the ossicular chain, Lab Anim. 43 (2009) 198–204.
[46] R.A. Chole, K. Kodama, Comparative histology of the tympanic membrane and its relationship to cholesteatoma, Annals of Otology, Rhinology & Laryngology. 98 (1989) 761–766.
[47] R. Aibara, J.T. Welsh, S. Puria, R.L. Goode, Human middle-ear sound transfer function and cochlear input impedance, Hear Res. 152 (2001) 100–109.
[48] P.L. Santa Maria, S.L. Redmond, M.D. Atlas, R. Ghassemifar, Histology of the healing tympanic membrane following perforation in rats, Laryngoscope. 120 (2010) 2061–2070.
[49] J. Van Hoorick, P. Gruber, M. Markovic, M. Tromayer, J. Van Erps, H. Thienpont, R. Liska, A. Ovsianikov, P. Dubruel, S. Van Vlierberghe, Cross-linkable gelatins with superior mechanical properties through carboxylic acid modification: increasing the two-photon polymerization potential, Biomacromolecules. 18 (2017) 3260–3272.

[50] A.P.S. Immich, P.C. Pennacchi, A.F. Naves, S.L. Felisbino, R.L. Boemo, S.S. Maria-Engler, L.H. Catalani, Improved tympanic membrane regeneration after myringoplastic surgery using an artificial biograft, Materials Science and Engineering: C. 73 (2017) 48–58.

Supplementary information

S.1. Li-TPO-L synthesis

LiBr (109 mmol) is dissolved in 150 ml butanone at 65°C while stirring. TPO-L (27.2 mmol) is added to the solution. The reaction mixture is stirred for 24 h at 65°C. The mixture is precipitated through suction filtration and washed with petroleum ether. The precipitate (~10 g) is dried under vacuum at RT.

S.2. ^{1}H-NMR spectrum of E-PCL

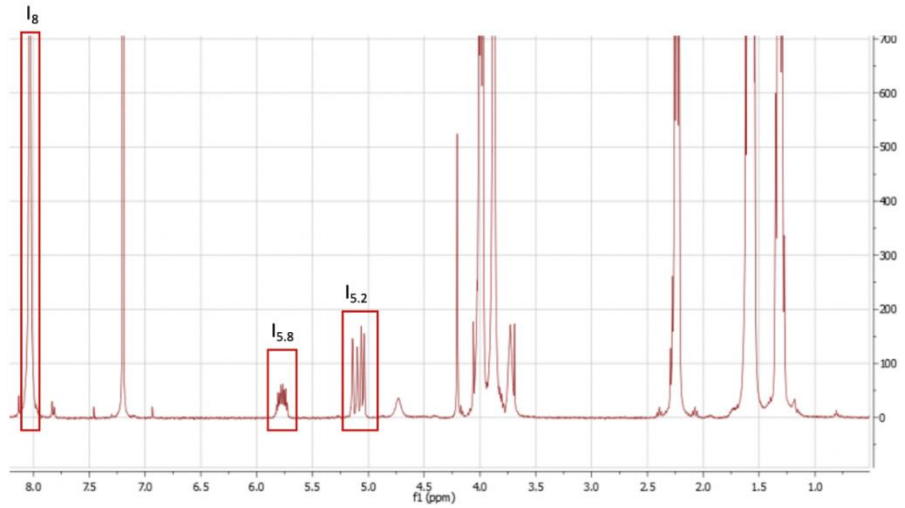

Figure S1: ^{1}H-NMR spectrum of E-PCL with the characteristic signals shown: I_8, $I_{5.8}$, $I_{5.2}$.

S.3. Absorbance spectrum PI/PA

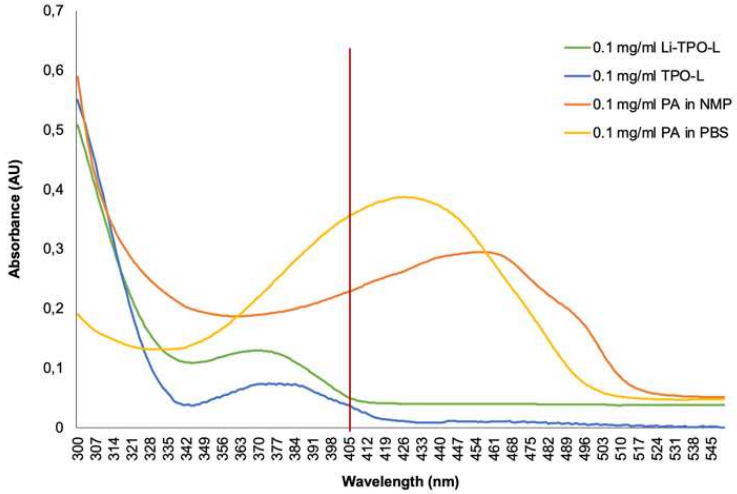

Figure S2: Absorption spectra of PI (Li-TPO-L/TPO-L) and PA (tartrazine) in PBS and/or NMP at a concentration of 0.1 mg/ml using UV-VIS spectroscopy.

S.4. DLP printer

S.4.1. DLP printer intensities

Table S1: LUMEN X power in mW/cm^2 at certain intensity percentages.

25%	30%	35%	40%	45%	50%	55%	60%	65%	70%	75%
7.26	9.94	12.31	14.80	17.20	19.51	21.56	23.72	25.72	27.75	29.52

Table S2: LUMEN X+ power in mW/cm^2 at certain intensity percentages.

25%	30%	35%	40%	45%	50%	55%	60%	65%	70%	75%
6.64	12.35	13.40	17.40	19.92	22.60	25.10	28.00	30.32	32.48	34.30

S.4.2. Conversion LUMEN X to LUMEN X+

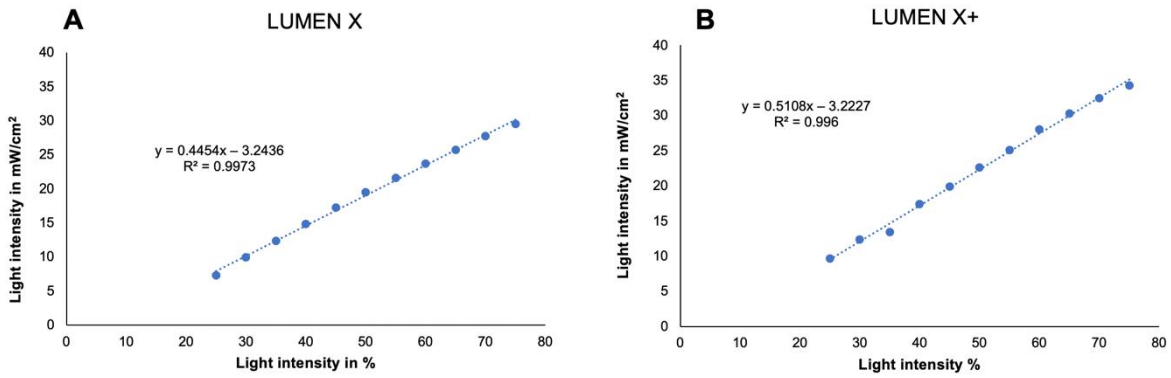

LIGHT INTENSITY	
100%	41.3 mW/cm²
75%	29.52 mW/cm²
50%	19.51 mW/cm²
30%	9.94 mW/cm²
25%	7.26 mW/cm²

CONVERSION FROM VALUES LUMEN X	
87%	41.3 mW/cm²
64%	29.52 mW/cm²
45%	19.51 mW/cm²
26%	9.94 mW/cm²
21%	7.26 mW/cm²

Figure S3: Conversion light intensity values from LUMEN X to LUMENX+ for the gelatins. (A) Values for LUMEN X, (B) Values for LUMEN X+.

S.4.3. Droplet tests

The droplet tests are performed on the LUMEN X DLP printer. The intensities are afterwards converted to the correlating intensities on the LUMENX+ DLP printer.

S.4.3.1. GelMA

Table S3: Results of the droplet test for 10 wt% GelMA in PBS with different PI concentrations on LUMENX. The amount of crosslinking is indicated as follows: (- - -) no crosslinking, (- -) slightly viscous, (-) viscous, (+) slightly crosslinked, (++) soft droplet, (+++) hard droplet.

Concentration	Li-TPO-L	Light intensity (%)	Exposure time (s)	Crosslinking
10 wt%	**0.01 wt%**	100%	3	
			5	- - -
			10	- - -
			15	
			20	- -
			25	
			30	-
Concentration	Li-TPO-L	Light intensity (%)	Exposure time (s)	Crosslinking
10 wt%	**0.1 wt%**	100%	3	

			5	- -
			10	- -
			15	-/+
			20	+
			25	++
			30	+++
		50%	3	
			5	
			10	
			15	
			20	
			25	
			30	
		75%	3	
			5	
			10	- - -
			15	- -
			20	
			25	+
			30	
Concentration	Li-TPO-L	Light intensity (%)	Exposure time (s)	Crosslinking
10 wt%	**1 wt%**	100%	3	++
			5	+++
			10	
			15	
			20	
			30	
		50%	3	
			5	++
			10	+++
			15	
			20	
			25	
			30	
		25%	3	
			5	
			10	+
			15	++
			20	+++
			25	
			30	
		75%	3	
			5	++/+++
			10	+++
			15	
			20	
			25	
			30	

Concentration	Li-TPO-L	Light intensity (%)	Exposure time (s)	Crosslinking
10 wt%	**2 wt%**	100%	3	++
			5	+++
			10	+++
			15	
			20	
			25	
			30	
		50%	3	
			5	+
			10	+++
			15	+++
			20	
			25	
			30	
		25%	3	- - -
			5	- -
			10	+
			15	++/+++
			20	+++
			25	
			30	
		75%	3	+
			5	++
			10	+++
			15	+++
			20	
			25	
			30	

Table S4: Results of the droplet test for 15 wt% GelMA in PBS with different PI concentrations on LUMENX. The amount of crosslinking is indicated as follows: (- - -) no crosslinking, (- -) slightly viscous, (-) viscous, (+) slightly crosslinked, (++) soft droplet, (+++) hard droplet.

Concentration	Li-TPO-L	Light intensity (%)	Exposure time (s)	Crosslinking
15 wt%	**0.01 wt%**	100%	3	
			5	- - -
			10	- - -
			15	- - -
			20	- -
			25	
			30	
Concentration	Li-TPO-L	Light intensity (%)	Exposure time (s)	Crosslinking
15 wt%	**0.1 wt%**	100%	3	
			5	+
			10	++
			15	+++

			20	
			25	
			30	
		50%	3	
			5	-
			10	-/+
			15	+
			20	++
			25	+++
			30	
		75%	3	
			5	- - -
			10	- -
			15	+
			20	+++
			25	+++
			30	
Concentration	Li-TPO-L	Light intensity (%)	Exposure time (s)	Crosslinking
15 wt%	**1 wt%**	100%	3	++
			5	+++
			10	
			15	
			20	
			25	
			30	
		50%	3	
			5	+/++
			10	+++
			15	
			20	
			25	
			30	
		25%	3	
			5	-
			10	++
			15	++
			20	+++
			25	
			30	
		75%	3	
			5	++
			10	+++

			15	
			20	
			25	
			30	
Concentration	Li-TPO-L	Light intensity (%)	Exposure time (s)	Crosslinking
15 wt%	**2 wt%**	100%	3	+++
			5	+++
			10	+++
			15	
			20	
			25	
			30	
		50%	3	++
			5	+++
			10	+++
			15	
			20	
			25	
			30	
		25%	3	- -
			5	+
			10	++
			15	+++
			20	
			25	
			30	
		75%	3	++/+++
			5	+++
			10	+++
			15	
			20	
			25	
			30	

Table S5: Results of the droplet test for 20 wt% GelMA in PBS with different PI concentrations on LUMENX. The amount of crosslinking is indicated as follows: (- - -) no crosslinking, (- -) slightly viscous, (-) viscous, (+) slightly crosslinked, (++) soft droplet, (+++) hard droplet.

Concentration	Li-TPO-L	Light intensity (%)	Exposure time (s)	Crosslinking
20 wt%	**0.01 wt%**	100%	3	
			5	+
			10	+
			15	++

			20	++
			25	++
			30	++
		50%	3	
			5	
			10	
			15	
			20	
			25	
			30	
		75%	3	
			5	--
			10	--
			15	+
			20	+
			25	++
			30	++
Concentration	Li-TPO-L	Light intensity (%)	Exposure time (s)	Crosslinking
20 wt%	**0.1 wt%**	100%	3	
			5	+/++
			10	++
			15	+++
			20	+++
			25	
			30	+++
		50%	3	
			5	-/+
			10	+
			15	++
			20	+++
			25	
			30	
		75%	3	
			5	+
			10	++
			15	+++
			20	+++
			25	
			30	
Concentration	Li-TPO-L	Light intensity (%)	Exposure time (s)	Crosslinking
20 wt%	**1 wt%**	100%	3	
			5	++/+++

			10	+++
			15	
			20	
			25	
			30	
		50%	3	
			5	++
			10	+++
			15	
			20	
			25	
			30	
		25%	3	
			5	-
			10	++
			15	+++
			20	
			25	
			30	
		75%	3	
			5	++/+++
			10	+++
			15	
			20	
			25	
			30	
Concentration	Li-TPO-L	Light intensity (%)	Exposure time (s)	Crosslinking
20 wt%	**2 wt%**	100%	3	
			5	++/+++
			10	+++
			15	
			20	
			25	
			30	
		50%	3	
			5	+
			10	++/+++
			15	+++
			20	
			25	
			30	
		25%	3	

			5	+
			10	++
			15	+++
			20	
			25	
			30	
		75%	3	
			5	++
			10	+++
			15	
			20	
			25	
			30	

Table S6: Results of the droplet test for 30 wt% GelMA in PBS with different PI concentrations on LUMENX. The amount of crosslinking is indicated as follows: (- - -) no crosslinking, (- -) slightly viscous, (-) viscous, (+) slightly crosslinked, (++) soft droplet, (+++) hard droplet.

Concentration	Li-TPO-L	Light intensity (%)	Exposure time (s)	Crosslinking
30 wt%	**0.01 wt%**	100%	3	
			5	++
			10	++
			15	++
			20	++
			25	+++
			30	
		50%	3	
			5	-/+
			10	++
			15	++
			20	++
			25	+++
			30	
		75%	3	
			5	+
			10	++
			15	+++
			20	+++
			25	
			30	
Concentration	Li-TPO-L	Light intensity (%)	Exposure time (s)	Crosslinking
30 wt%	**0.1 wt%**	100%	3	
			5	++

			10	+++
			15	+++
			20	
			25	
			30	
		50%	3	
			5	++
			10	+++
			15	+++
			20	
			25	
			30	
		75%	3	
			5	++
			10	+++
			15	+++
			20	
			25	
			30	
Concentration	Li-TPO-L	Light intensity (%)	Exposure time (s)	Crosslinking
30 wt%	**1 wt%**	100%	3	
			5	+++
			10	
			15	
			20	
			25	
			30	
		50%	3	
			5	++/+++
			10	+++
			15	
			20	
			25	
			30	
		25%	3	
			5	++
			10	+++
			15	
			20	
			25	
			30	
		75%	3	

			5	++/+++
			10	+++
			15	
			20	
			25	
			30	
Concentration	Li-TPO-L	Light intensity (%)	Exposure time (s)	Crosslinking
30 wt%	**2 wt%**	100%	3	+++
			5	+++
			10	
			15	
			20	
			25	
			30	
		50%	3	++/+++
			5	+++
			10	
			15	
			20	
			25	
			30	
		25%	3	
			5	++
			10	+++
			15	
			20	
			25	
			30	
		75%	3	++/+++
			5	+++
			10	
			15	
			20	
			25	
			30	

S.4.3.2. E-PCL

Table S7: Results of the droplet test for 50 wt% E-PCL with PETA4SH in NMP with different PI concentrations on LUMENX. The amount of crosslinking is indicated as follows: (- - -) no crosslinking, (- -) slightly viscous, (-) viscous, (+) slightly crosslinked, (++) soft droplet, (+++) hard droplet.

Concentration	TPO-L	Light intensity (%)	Exposure time (s)	Crosslinking
50 wt%	**0.1 wt%**	100%	3	
			5	
			10	
			15	
			20	
			25	
			30	---
Concentration	TPO-L	Light intensity (%)	Exposure time (s)	Crosslinking
50 wt%	**1 wt%**	100%	3	
			5	
			10	
			15	
			20	
			25	
			30	---
Concentration	TPO-L	Light intensity (%)	Exposure time (s)	Crosslinking
50 wt%	**1.25 wt%**	100%	3	
			5	
			10	
			15	
			20	
			25	
			30	---
Concentration	TPO-L	Light intensity (%)	Exposure time (s)	Crosslinking
50 wt%	**2.5 wt%**	100%	3	
			5	
			10	
			15	
			20	
			25	
			30	-+

Table S8: Results of the droplet test for 60 wt% E-PCL with PETA4SH in NMP with different PI concentrations on LUMENX. The amount of crosslinking is indicated as follows: (- - -) no crosslinking, (- -) slightly viscous, (-) viscous, (+) slightly crosslinked, (++) soft droplet, (+++) hard droplet.

Concentration	TPO-L	Light intensity (%)	Exposure time (s)	Crosslinking
60 wt%	**0.1 wt%**	100%	3	
			5	
			10	
			15	
			20	
			25	
			30	---
Concentration	TPO-L	Light intensity (%)	Exposure time (s)	Crosslinking
60 wt%	**1 wt%**	100%	3	
			5	
			10	
			15	
			20	
			25	
			30	---
Concentration	TPO-L	Light intensity (%)	Exposure time (s)	Crosslinking
60 wt%	**1.25 wt%**	100%	3	
			5	
			10	
			15	
			20	
			25	
			30	---
Concentration	TPO-L	Light intensity (%)	Exposure time (s)	Crosslinking
60 wt%	**2.5 wt%**	100%	3	
			5	
			10	
			15	+
			20	++
			25	+++
			30	
		50%	3	
			5	
			10	
			15	---
			20	--/-+
			25	+
			30	++/+++

		25%	3	
			5	
			10	
			15	
			20	
			25	
			30	
		75%	3	
			5	
			10	
			15	+
			20	++
			25	+++
			30	

Table S9: Results of the droplet test for 70 wt% E-PCL with PETA4SH in NMP with different PI concentrations on LUMENX. The amount of crosslinking is indicated as follows: (- - -) no crosslinking, (- -) slightly viscous, (-) viscous, (+) slightly crosslinked, (++) soft droplet, (+++) hard droplet.

Concentration	TPO-L	Light intensity (%)	Exposure time (s)	Crosslinking
70 wt%	**0.1 wt%**	100%	3	
			5	
			10	
			15	
			20	
			25	
			30	---
Concentration	TPO-L	Light intensity (%)	Exposure time (s)	Crosslinking
70 wt%	**1 wt%**	100%	3	
			5	
			10	
			15	
			20	
			25	
			30	---
Concentration	TPO-L	Light intensity (%)	Exposure time (s)	Crosslinking
70 wt%	**1.25 wt%**	100%	3	
			5	---/--
			10	--/-
			15	+/++
			20	++

			25	+++
			30	
		50%	3	
			5	
			10	---
			15	--/+
			20	+/++
			25	++/+++
			30	++/+++
		25%	3	
			5	
			10	
			15	
			20	
			25	
			30	
		75%	3	
			5	---
			10	--/-+
			15	+
			20	++/+++
			25	+++
			30	
Concentration	TPO-L	Light intensity (%)	Exposure time (s)	Crosslinking
70 wt%	**2.5 wt%**	100%	3	
			5	
			10	
			15	++
			20	+++
			25	
			30	
		50%	3	
			5	
			10	
			15	---
			20	--/-+
			25	+
			30	++/+++
		25%	3	
			5	
			10	

			15	
			20	
			25	
			30	
		75%	3	
			5	
			10	
			15	++
			20	++/+++
			25	+++
			30	

S.5. *In situ* photo-rheology

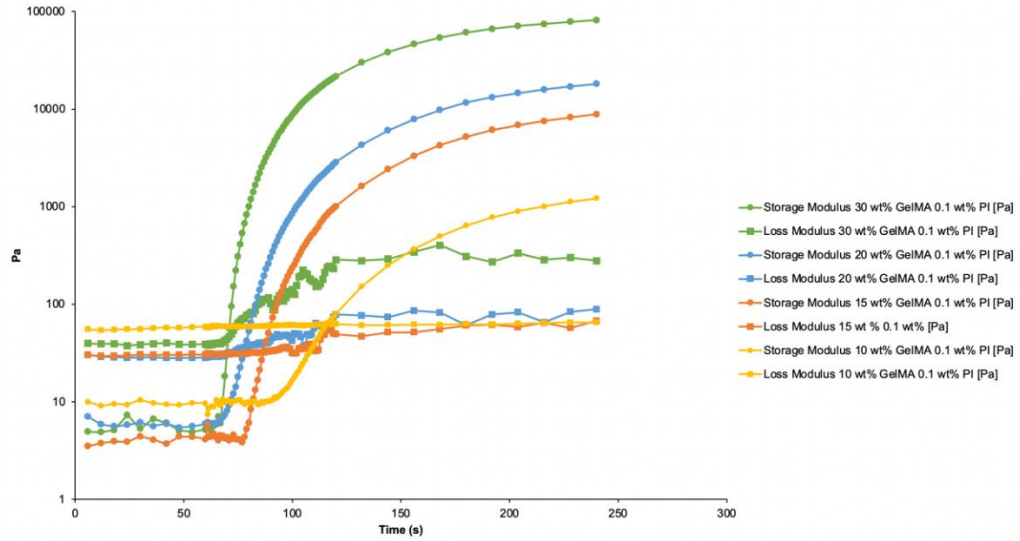

Figure S4: Overview of loss and storage moduli of 10, 15, 20, 30 wt% GelMA with 0.1 wt% Li-TPO-L.

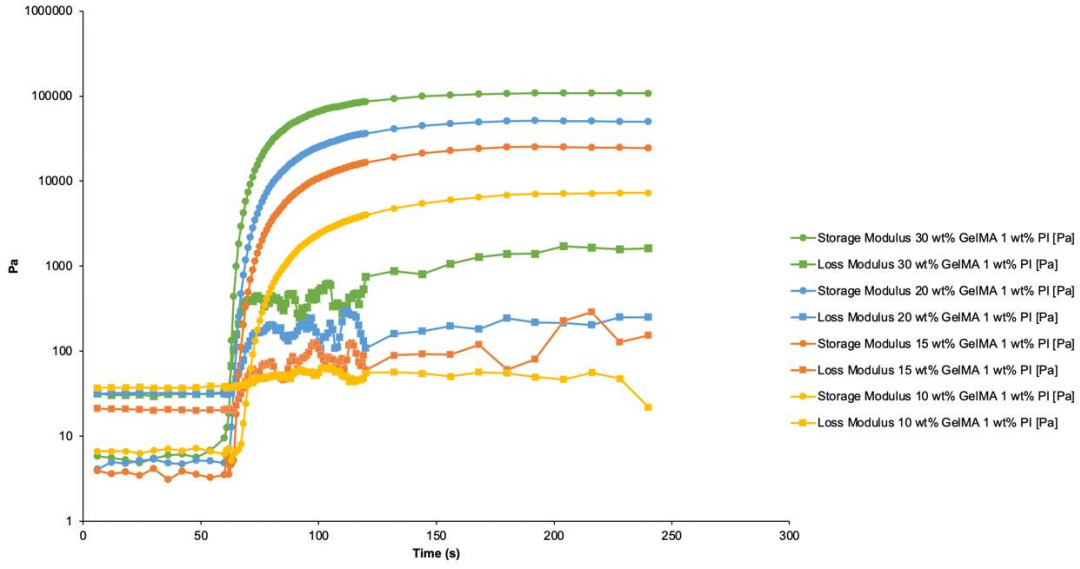

Figure S5: Overview of loss and storage moduli of 10, 15, 20, 30 wt% GelMA with 1 wt% Li-TPO-L.

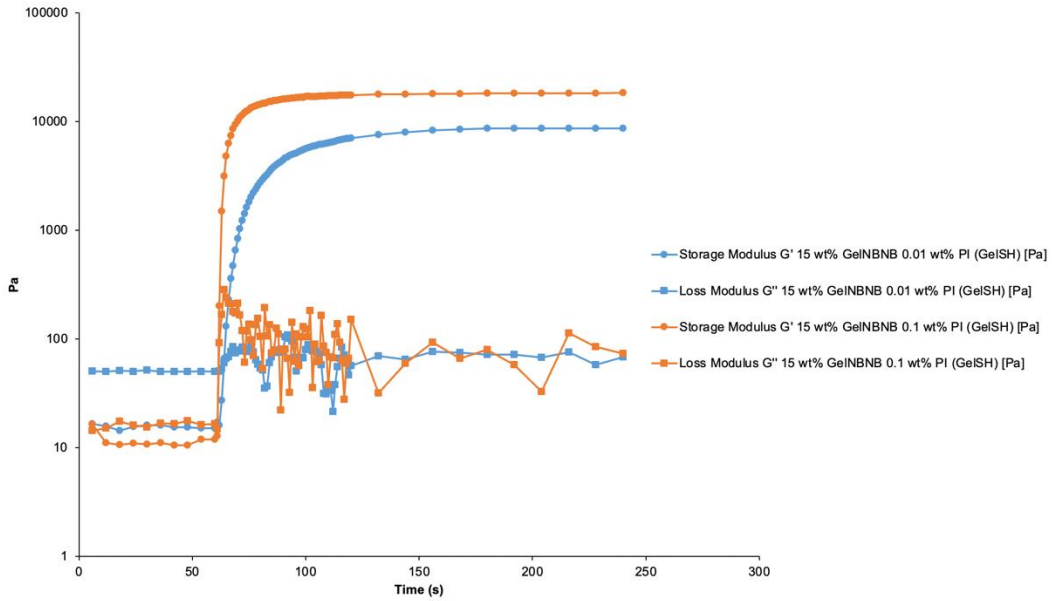

Figure S6: Overview of loss and storage moduli of 15 wt% GelNBNB-GelSH with 0.01 and 0.1 wt% Li-TPO-L.

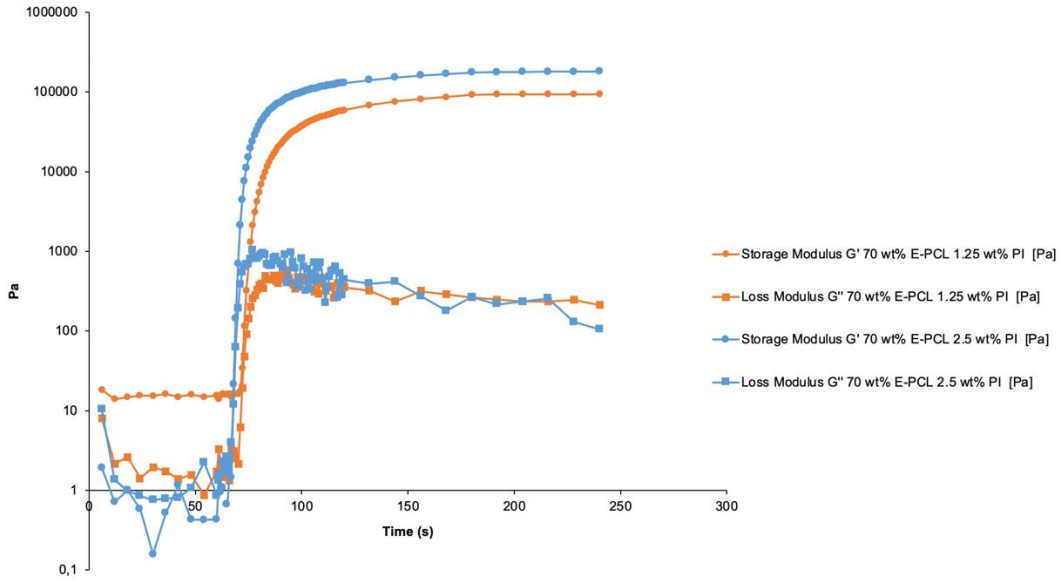

Figure S7: Overview of loss and storage moduli of 70 wt% E-PCL with 1.25 and 2.5 wt% TPO-L.

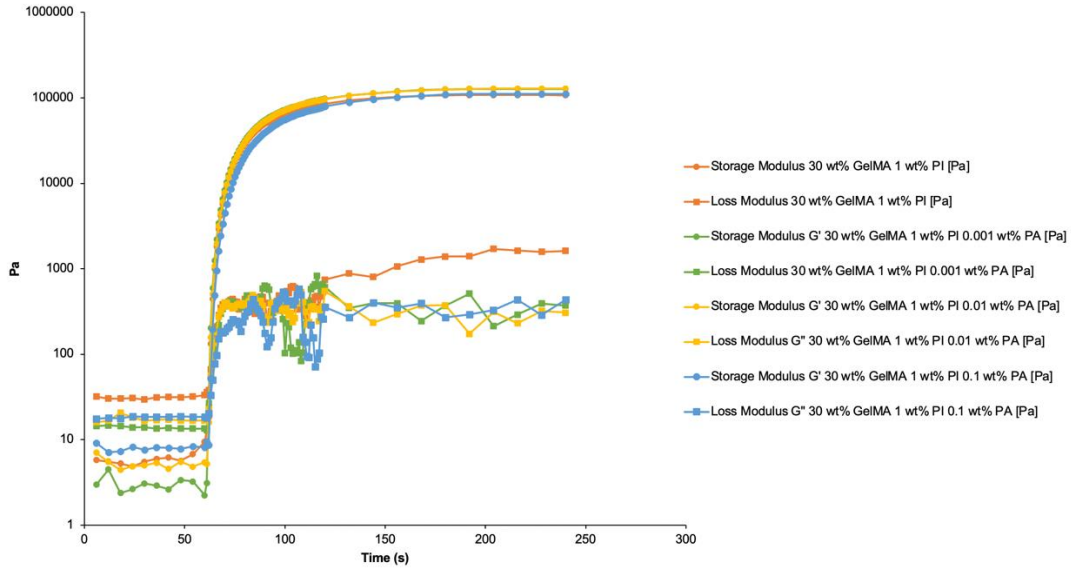

Figure S8: Overview of loss and storage moduli of 30 wt% GelMA with 1 wt% Li-TPO-L and 0.001, 0.01 or 0.1 wt% PA.

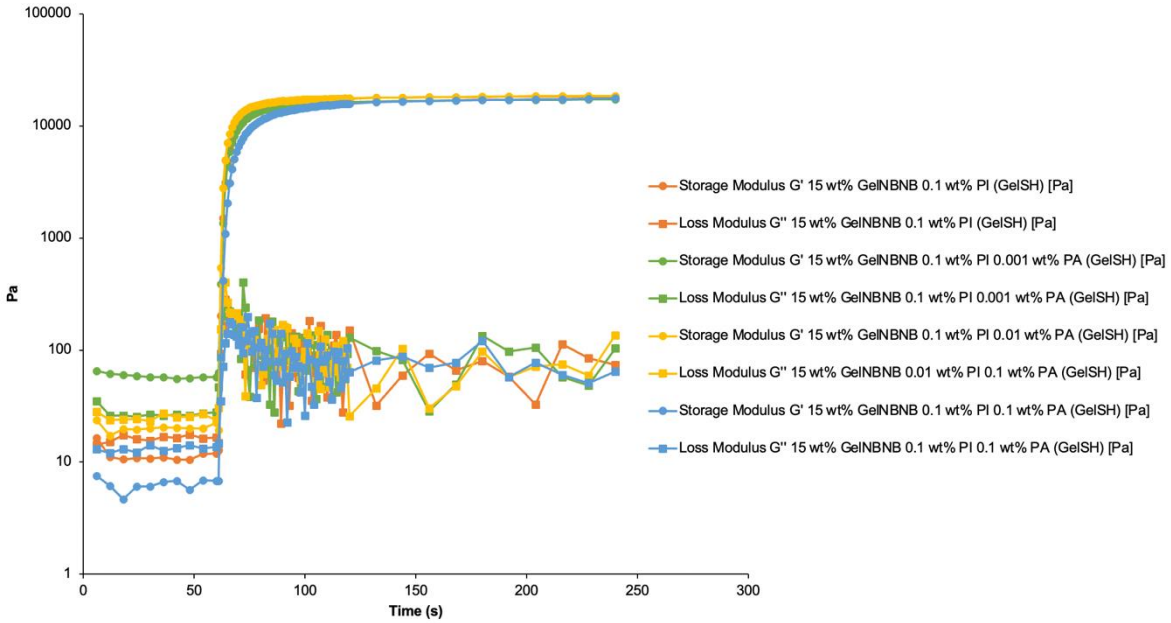

Figure S9: Overview of loss and storage moduli of 15 wt% GelNBNB-GelSH (0.5 eq TCEP) with 0.1 wt% Li-TPO-L and 0.001, 0.01 or 0.1 wt% PA.

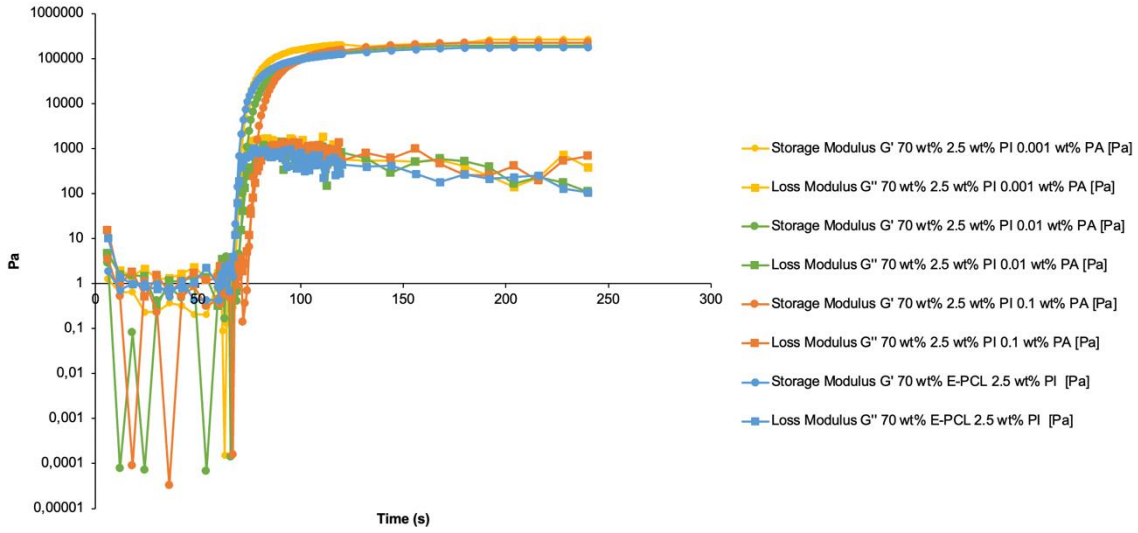

Figure S10: Overview of loss and storage moduli of 70 wt% E-PCL-PETA4SH with 2.5 wt% TPO-L and 0.001, 0.01 or 0.1 wt% PA.

S.6. *In vitro* evaluation

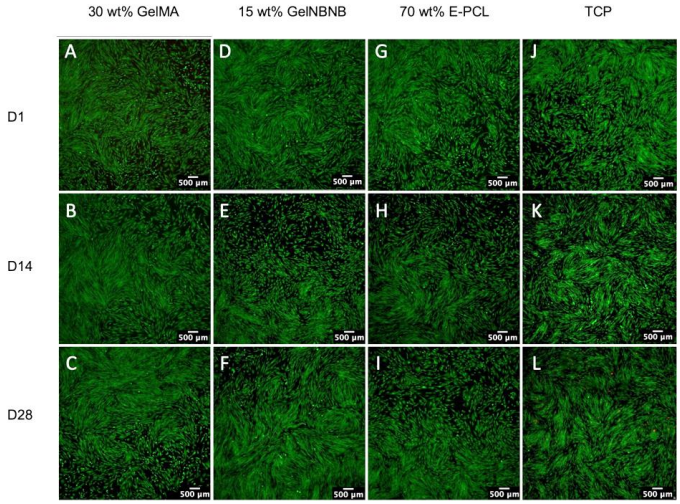

Figure S11: Indirect fibroblast viability assay through fluorescence microscopy of living (green) and dead (red) cells on medium in contact with 30 wt% GelMA prints (A (D1), B (D14) and C (D28)), 15 wt% GelNBNB prints (D (D1), E (D14) and F (D28)), 70 wt% E-PCL prints (G (D1), H (D14) and I (D28)) and tissue culture plate (TCP) (images taken at 4x magnification and scale bar = 500 µm).

S.7. *In vivo* and *ex vivo* evaluation

S.7.1. Endoscopic implantation procedure

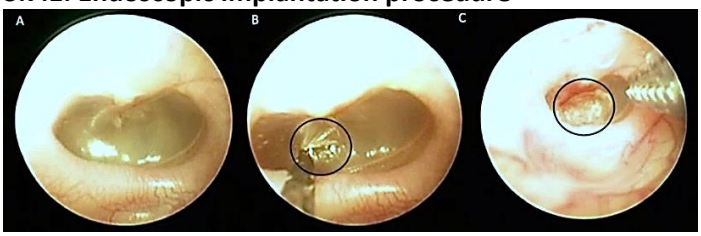

Figure S12: The endoscopic implantation procedure. (A) Healthy TM before perforation, (B) acute TM perforation made with a 23G needle, (C) implantation of a scaffold covering the acute TM perforation.

S.7.2. Endoscopy after four weeks

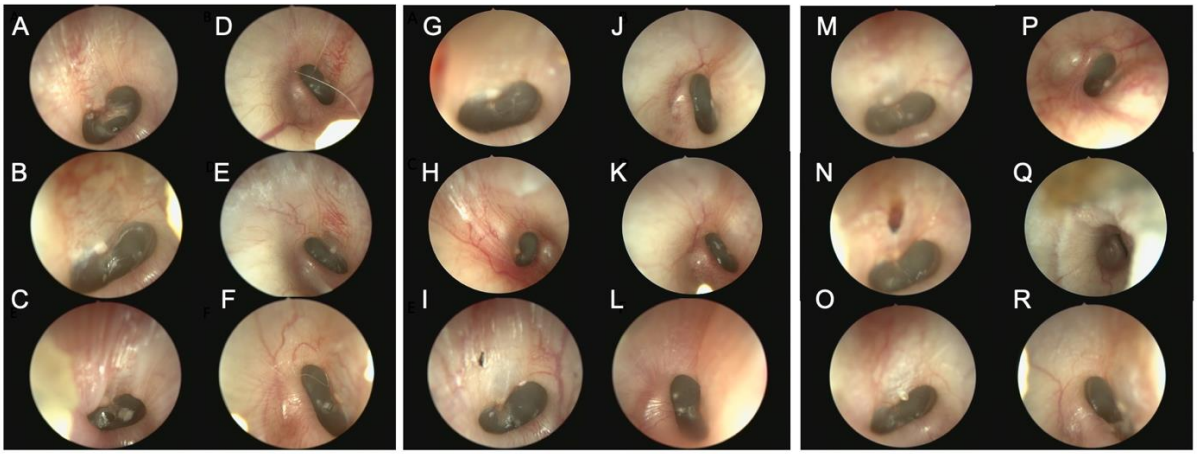

Figure S13: Endoscopy images taken after four weeks of implantation. (A-F) GelNBNB experimental group: (A) K8L, (B) K2L, (C) K4L, (D) K8R (E) K2R and (F) K4R. (G-L) GelMA experimental group: (G) K12L, (H) K3L, (I) K14L, (J) K12R, (K) K3R and (L) K14R. (M-R) E-PCL experimental group: (M) K11L, (N) K9L, (O) K6L, (P) K11R, (Q) K9R and (R) K6R.

S.7.3. Microscopy after four weeks

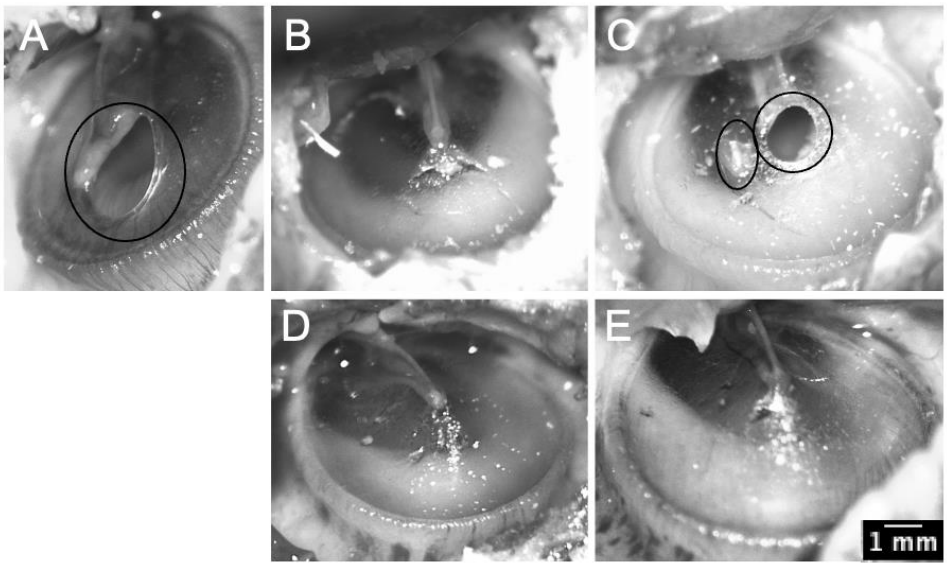

Figure S14: Images taken during dissection with a surgical microscope. (A-C) Left TMs with GelNBNB scaffold implanted, (D-E) perforated controls. Codes: (A) K8L, (B) K2L, (C) K4L, (D) K2R, (E) K4R. Scale bar = 1 mm.

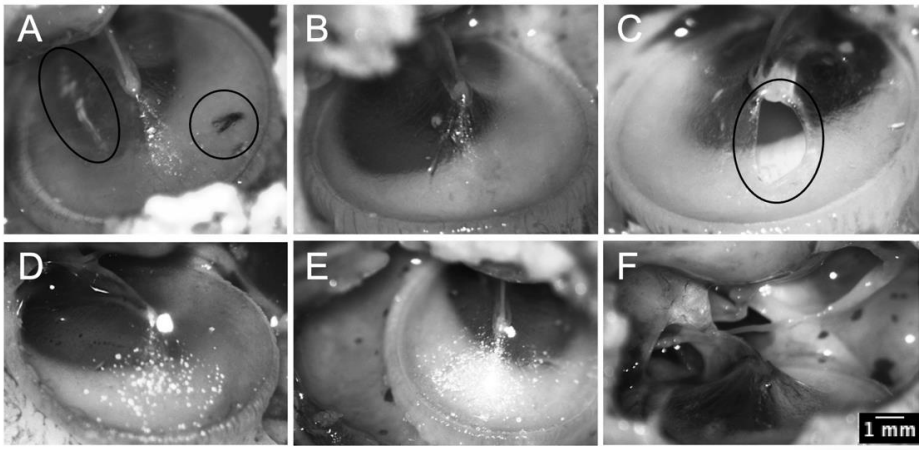

Figure S15: Images taken during dissection with a surgical microscope. (A-C) left TMs with GelMA scaffold implanted, (D) healthy control, (E-F) perforated controls. Codes: (A) K12L, (B) K3L, (C) K14L (D) K12R, (E) K3R, (F) K14R. Scale bar = 1 mm.

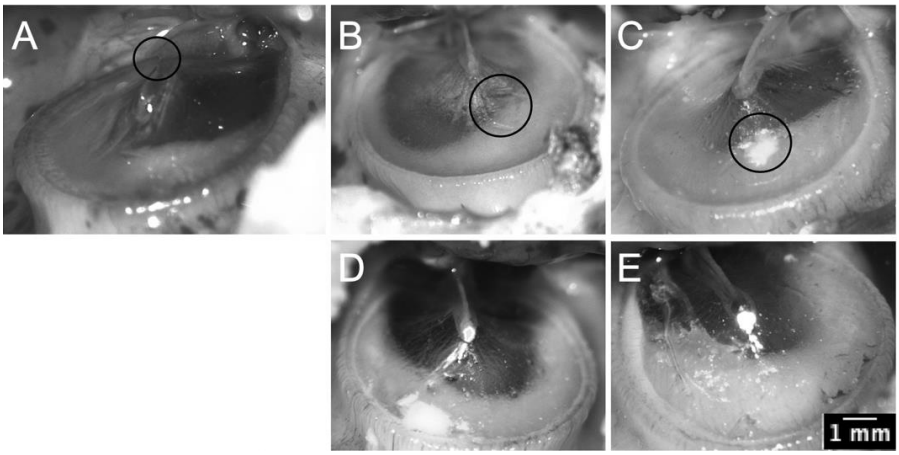

Figure S16: Images taken during dissection with a surgical microscope. (A-C) left TMs with E-PCL scaffold implanted, (D&E) perforated controls. Codes: (A) K11L, (B) K9L, (C) K6L, (D) K9R, (E) K6R. Scale bar = 1 mm.

S.7.4. LDV

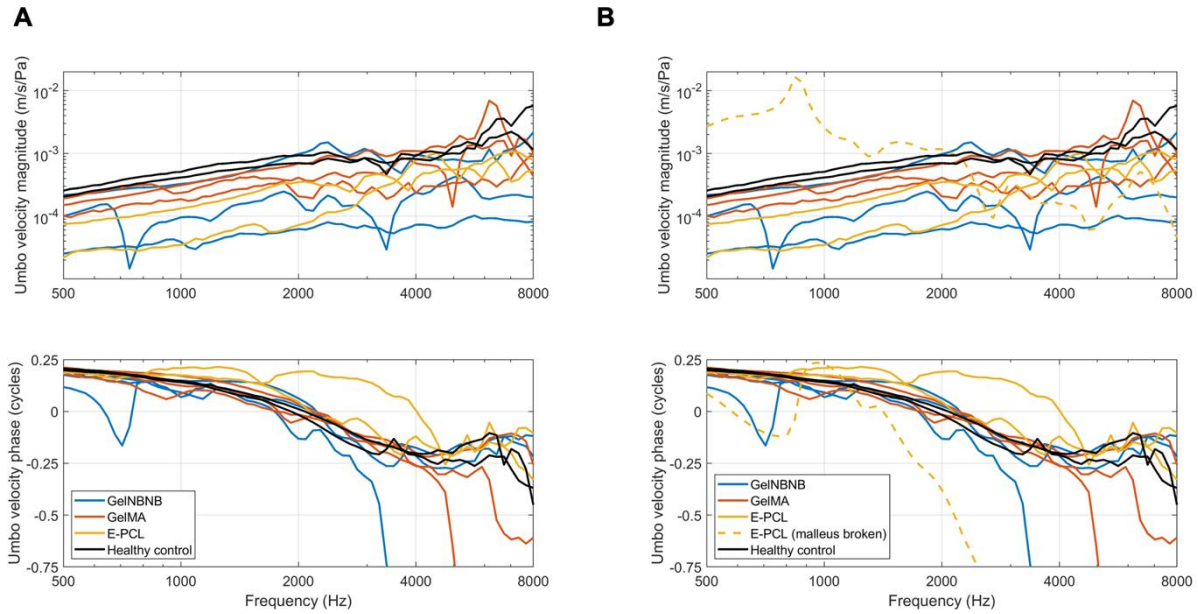

Figure S17: LDV plots with an overview of velocity magnitude (m/s/Pa) and phase (cycles) response of all left samples with (B) and without (A) sample K11L which had a broken malleus (shown in yellow dashed line).

S.7.5. DIC

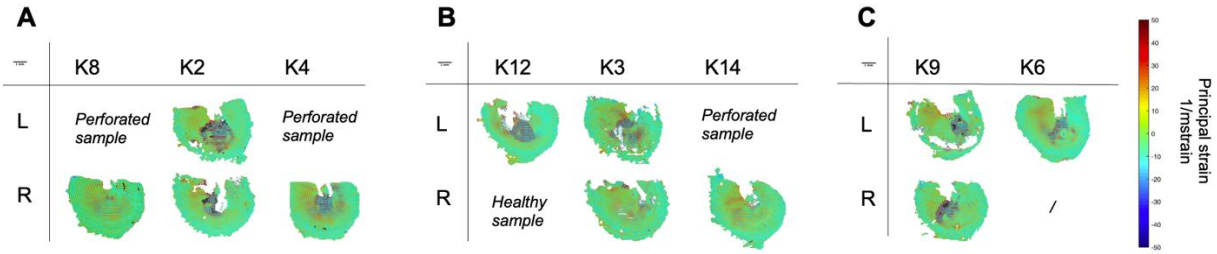

Figure S18: DIC measurements showing the principal strain of left and right samples in (A) GelNBNB experimental group, (B) GelMA experimental group and (C) E-PCL experimental group. Strain magnitude is represented by color correlating to the color scale. Scale bar = 1 mm.

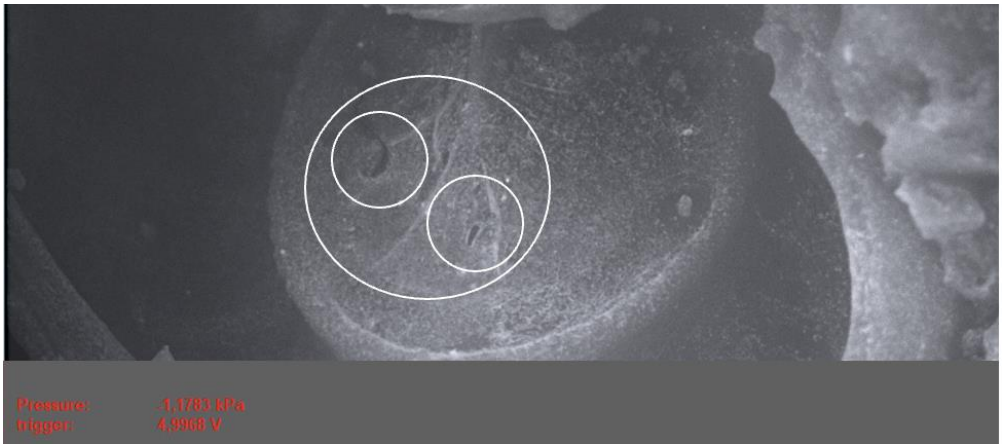

Figure S19: Under-pressure image of sample K2R showing two small perforations and wrinkling of the TM. Image is taken at an under-pressure of -1.1783 kPa.

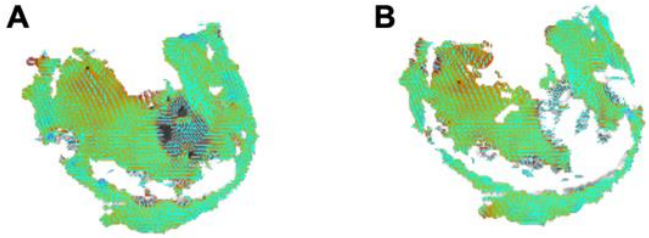

Figure S20: DIC images at a positive pressure of 2kPa at time point (A) 8 and (B) 50.

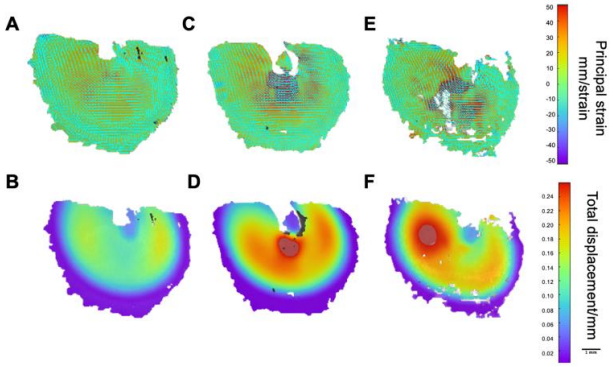

Figure S21: Principal strain and total displacement visualization of samples (A-B) control K8R, (C-D) K4R and (E-F) K3L. The scale bar of principal strain (mm/strain) and total displacement/mm are included. Scale bar = 1 mm.

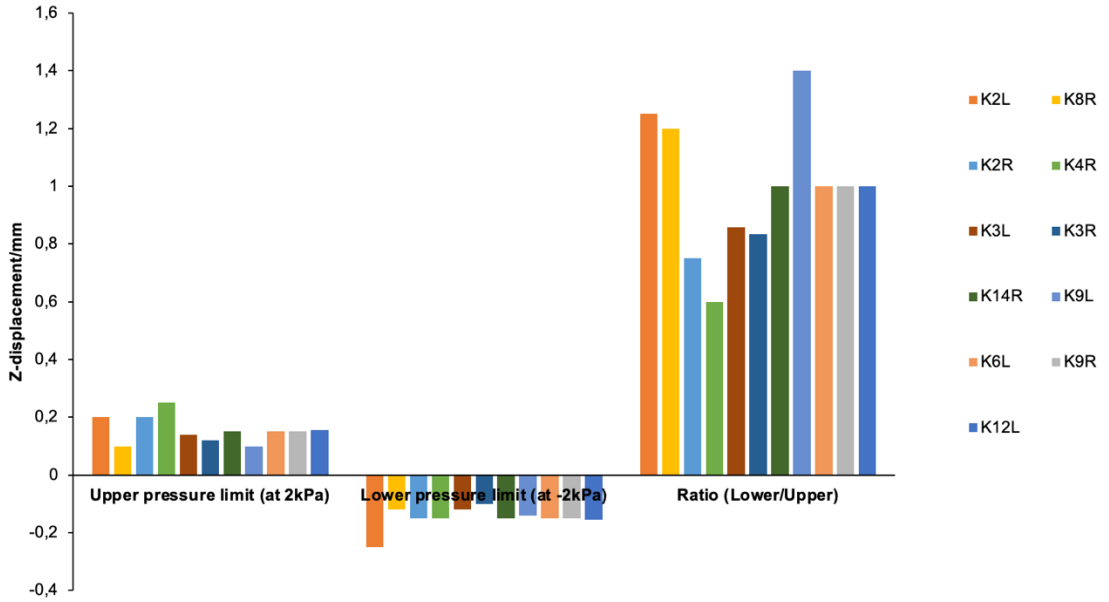

Figure S22: Z-displacement values measured at lower and upper pressure limit using DIC for every sample and the corresponding ratio of the lower to upper pressure limit at -2 kPa and 2 kPa respectively.

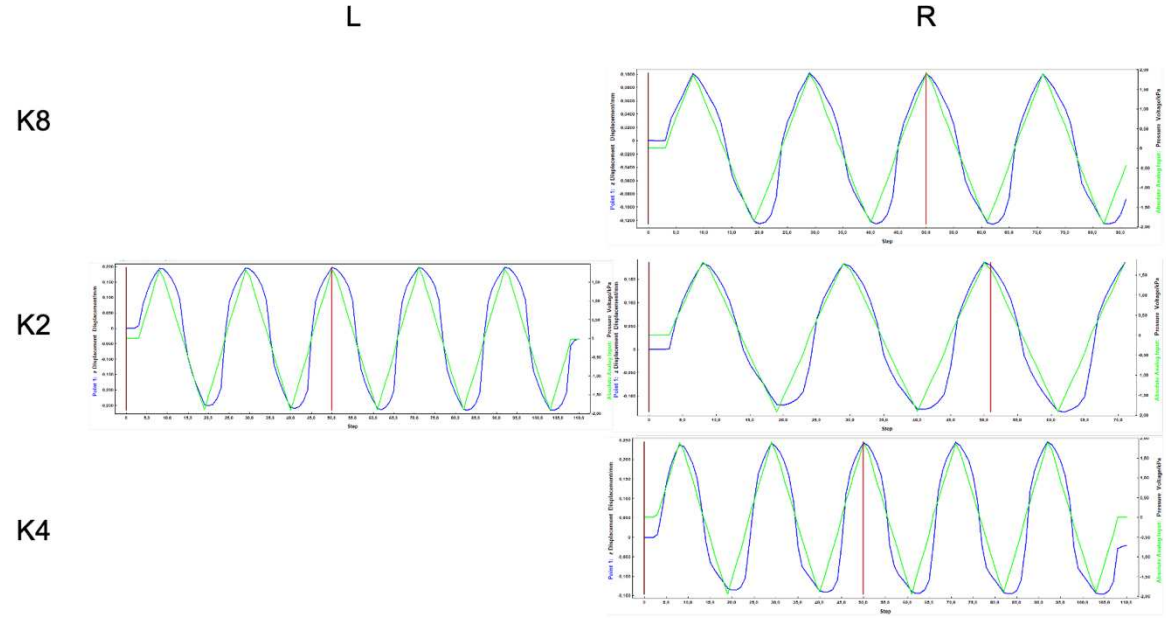

Figure S23: Umbo Z-displacement per mm as function at certain linearly increasing pressure voltage (kPa) ranging between -2kPa until 2kPa at a pressure rate of 0.25 kPa/s. Z-displacement patterns of GelNBNB experimental group including K8R, K2L, K2R and K4R.

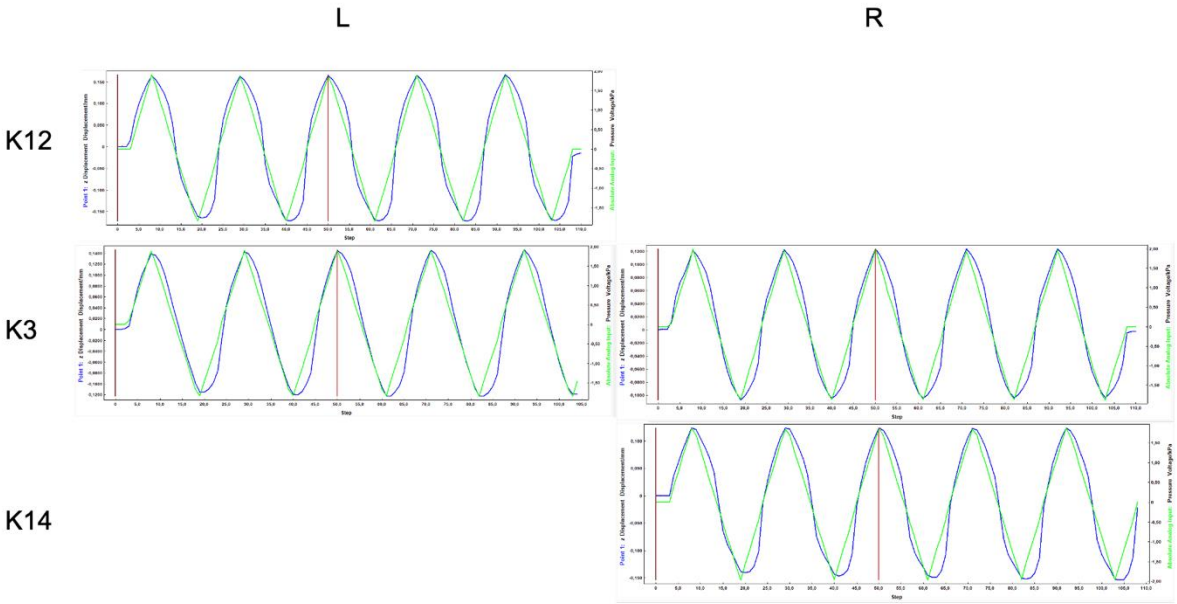

Figure S24: Umbo Z-displacement per mm as function at certain linearly increasing pressure voltage (kPa) ranging between -2kPa until 2kPa at a pressure rate of 0.25 kPa/s. Z-displacement patterns of GelMA experimental group including K12L, K3L, K3R and K14R.

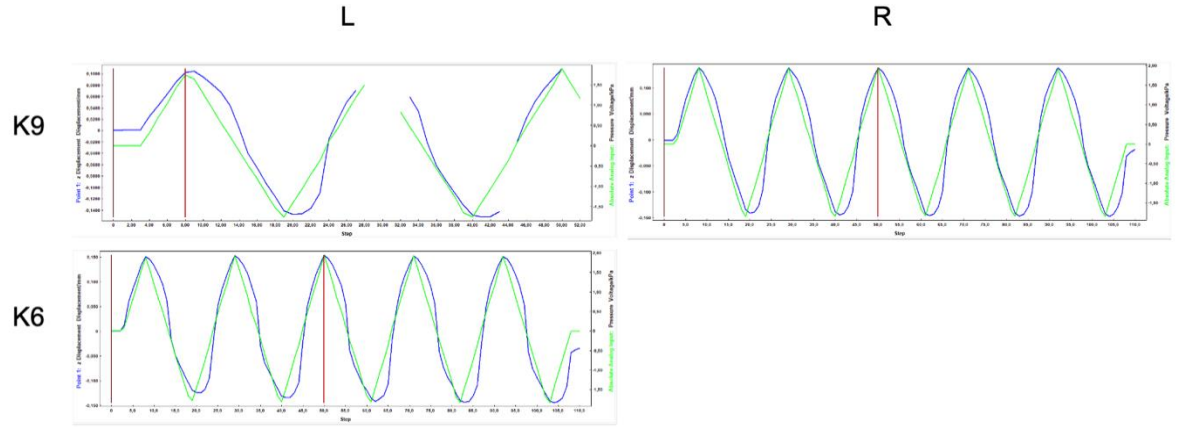

Figure S25: Umbo Z-displacement per mm as function at certain linearly increasing pressure voltage (kPa) ranging between -2kPa until 2kPa at a pressure rate of 0.25 kPa/s. Z-displacement patterns of E-PCL experimental group including K9L, K9R a nd K6L.